Monthly Notices
of the
ROYAL ASTRONOMICAL SOCIETY

MNRAS **523,** 2858–2875 (2023) https://doi.org/10.1093/mnras/stad1518
Advance Access publication 2023 May 19

Chemical evolution of electron-bombarded crystalline water ices at different temperatures using the PROCODA code

S. Pilling,[★] C. H. da Silveira and A. Ojeda-Gonzalez
Instituto de Pesquisa e Desenvolvimento, Universidade do Vale do Paraíba, São José dos Campos 12244-000, SP, Brazil

Accepted 2023 May 16. Received 2023 May 15; in original form 2023 March 27

ABSTRACT

Water ices are a common component of cold space environments, including molecular and protostellar clouds, and the frozen surfaces of moons, planets, and comets. When exposed to ionizing and/or thermal processing, they become a nursery for new molecular species and are also responsible for their desorption to the gas-phase. Crystalline water ice, produced by the deposition of gaseous water at warm (80–150 K) surfaces or by the heating of cold amorphous water ice (up to ∼150 K), is also regularly detected by astronomical observations. Here, we employed the PROCODA code to map the chemical evolution of 5 keV electron-bombarded crystalline water-ices at different temperatures (12, 40, 60 and 90 K). The chemical network considered a total of 61 coupled reactions involving nine different chemical species within the ice. Among the results, we observe that the average calculated effective rate constants for radiation-induced dissociation decrease as the ice´s temperature increases. The abundance of molecular species in the ice at chemical equilibrium and its desorption to gas-phase depend on both the temperature of the ice. H_2O molecules are the dominant desorbed species, with a desorption yield of about 1 molecule per 100 electrons, which seems to be enhanced for warmer crystalline ices. The obtained results can be employed in astrochemical models to simulate the chemical evolution of interstellar and planetary environments. These findings have implications for astrochemistry and astrobiology, providing insight into crucial chemical processes and helping us understand the chemistry in cold regions in space.

Key words: astrochemistry – molecular data – molecular processes – methods: data analysis – software: data analysis – ISM: molecules.

1 INTRODUCTION

The interstellar medium (ISM) is a vast region of space filled with atomic and molecular gas, dust, ices, and is the birthplace of stars and planets. Water (rich) ices are an important component of the ISM, as they are the main source of oxygen and other elements necessary for the formation of stars and planets. In the colder and denser regions of the ISM the temperature can be as low as 5–10 K and the ice is preferentially in the amorphous form (a disordered form of water ice). However, due to ongoing star formation, associated to denser clouds and protostellar environments, amorphous ices can be heated and suffer morphological changes, allowing the appearance of crystalline water ices (e.g. Jenniskens & Blake 1996; Jenniskens et al. 1998; Hansen & McCord 2004; Ladd-Parada et al. 2022). A good review on amorphous and crystalline astrophysical ices can be obtained from Kouchi et al. (1994).

Besides thermal heating, the astrophysical ices are also exposed to ionizing radiation from galactic and extragalactic sources. This includes UV, X-rays, cosmic rays, and energetic electrons that drive the chemistry in and on the ice and also promote ice to gas-phase desorption processes. The energy delivered by radiation allows the enhancement of molecular complexity in the ices and also the appearance of new gas-phase molecules in the ISM (e.g. Andrade et al. 2008; Nuevo et al. 2008; Pilling et al. 2009, 2010b, 2012; de Marcellus et al. 2011; Pilling & Berganti 2015; Garcia et al. 2019; Herbst & Garrod 2022). Astronomical observations using the Atacama Large Millimeter/submillimeter Array (ALMA) and the *James Webb Space Telescope* (*JWST*) have revealed the variety of molecular species present in cold, radiation-rich environments (e.g. Walsh et al. 2014, Podio et al. 2019; Ilee et al. 2021; Yang et al. 2022; McClure et al. 2023; and references therein).

Crystalline water has been found in several regions of space, including comets, frozen moons of giant planets, interstellar clouds, and protoplanetary discs (e.g. Smoluchowski 1983; Prialnik & Bar-Nun 1992; Malfait et al. 1999; Schmidt & Dahl-Jensen 2003; Gibb et al. 2004; Jewitt & Luu 2004; Hansen & McCord 2004; Dartois 2005; Emery et al. 2005; Brown et al. 2006; Justtanont et al. 2006; Lunine, 2006; Cook et al. 2007; Boogert et al. 2008; Öberg et al. 2011; Lombaert et al. 2013; Suh & Kwon 2013; Barucci et al. 2015; Mousis et al. 2016; Berdis et al. 2020). In the laboratory, the chemical changes induced by radiation on crystalline water ices have been studied by several groups (e.g. Moore & Hudson 1992, Strazzulla et al. 1992, Johnson & Quickenden 1997; Mastrapa & Brown 2006; Zheng et al. 2006, 2007, Famá et al. 2010, Piling et al. 2011; Dartois et al. 2015; Teolis et al. 2017; Mifsud et al. 2022a, b; Mejía et al. 2022; and references therein).

It is worth noting that the bombardment by cosmic rays on crystalline water ice also promotes amorphyzation processes in the astrophysical ices (e.g. Moore & Hudson, 1992; Strazzulla et al. 1992, Famá et al. 2010; Dartois et al. 2015). Such phenomena has also been observed when ices is irradiated by ionizing photons but

---

★ E-mail: sergiopilling@yahoo.com.br

Published by Oxford University Press on behalf of Royal Astronomical Society

with low intensity (e.g. Kouchi & Kuroda 1990; Leto & Barata 2003). Additionally, the amorphyzation of crystalline water ices can also lead to an increase in the porosity of the ices, which can affect ices' ability to store and transport molecules. This can have a significant effect on the transport of molecules within the ices, which can be important for the formation of complex organic molecules. A detailed discussion on this process can be obtained at Dartois et al. (2015) and references therein.

This study simulated the effects of electron and ionic components of cosmic rays on crystalline water ices at different temperatures, resembling bombardment by electrons from stellar wind, galactic, and extragalactic sources. Fast secondary electrons produced by protons and other ionic components are the primary agents inducing chemical changes within the irradiated ices, as discussed in previous works (e.g. Paranicas et al. 2001; Zheng et al. 2006; Pilling et al. 2010a; 2011; Plainaki et al. 2012; Pilling & Bergantini 2015).

In the current manuscript, we focus on the chemical kinetics of electron-bombarded crystalline water ice and the changes induced by the ice temperature during this process. We employ the PROCODA code (see also Pilling et al. 2022, 2023) to map the chemical evolution and characterize the chemical equilibrium (CE) of crystalline water ices at temperatures of 12, 40, 60, and 90 K, under bombardment of 5 keV electrons. The experimental data were obtained from Zheng et al. (2006). The PROCODA code solves a system of coupled differential equations and describes the evolution of the molecular abundances with the irradiation time for ices under processing by radiation. This code has been employed previously to investigate the changes induced by radiation at pure CO_2, CO, acetonitrile, and H_2O ices (Carvalho et al. 2022; Pilling et al. 2022, 2023; Pilling et al., in preparation; Da Silveira & Pilling, in preparation).

Section 2 of this work describes the computational methodology and details of the experimental data used, taken from the literature. Section 3 presents the results, with an emphasis on the calculated reaction rates as well as comparisons between previous works on amorphous water, and ends with an extended discussion on the CE phase. Some astrophysical implications are given in Section 4. Finally, Section 5 provides the conclusions and final remarks.

2 METHODOLOGY

In this study, we use the PROCODA code (see also Pilling et al. 2022, 2023) to explore the chemical evolution of crystalline H_2O ice under irradiation by energetic electrons with energies of 5 keV. We calculate the effective rate constants (ERCs) and characterize the CE phase that occurs at higher radiation fluences. As discussed in detail in the previous manuscripts, the term 'effective' in the rate constant is used to account for the various chemical environments in which a given reaction can occur within the ice.

2.1. Experimental data set

The experimental data set considered here was taken from Zheng et al. (2006) and describes the irradiation of crystalline water ice by 5 keV electrons at four different temperatures: 12, 40, 60, and 90 K. The employed ice thickness was about 115 nm prepared by condensing water vapor onto the silver substrate at 140 K, which was then chilled down until the temperature of irradiation. From the experimental work, we obtained the column densities of the species H_2, O_2, H_2O, H_2O_2, and O_3 (estimated to be very low). The column densities of H_2O and H_2O_2 were measured *in situ* by a Fourier transform infrared (IR) spectrometer (Nicolet 510 DX FTIR) and the column densities of H_2 and O_2 were estimated by the authors from the species subliming from the ice monitored with a quadrupole mass spectrometer (Balzer QMG 420). It is worth noting that in this manuscript we consider all these five species as 'observed' (including the O_3) to avoid confusion with the other species considered in the chemistry model named 'non-observed', as we will see later on. The experimental uncertainty in the column density was below 30 per cent (Zheng et al. 2006).

For numerical purposes, we consider O_3 an 'observed' species having a non-zero column density. We adopt a very low value for its column density (a virtually negligible value of ~4e8 molecules cm^{-2}; below the detection limit of the spectrometer). As will be presented in the results section, even considering the very low amount of ozone initially and the fact that this species participates in several reactions, the abundance of ozone still remains very low until the end of irradiation (below IR spectrometer detection limits). It is worth noting that besides this species not being detected in this pure water-ice irradiation experiment, it was easily detected in other bombarded water-rich ices (e.g. Teolis et al. 2006; Pilling et al. 2010a, b; Mejía et al. 2022). The production of ozone from the irradiation of water ices is a hot topic in astrochemistry and solid-state chemistry, and this issue should be carefully investigated in future publications.

A discussion is needed to explain the column densities of H_2 and O_2 measured by Zheng et al. (2006). The column densities of these species were estimated by the authors from the measurements of related desorbed molecules (H, H_2, O, and O_2) from the ice during experiments, performed by employing mass spectroscopy. According to the authors, the uncertainty in this process was usually below 30 per cent.

The experimental data considered were obtained from samples irradiated at a maximum fluence of 1.7e21 eV cm^{-2} (~180 min of irradiation) by employing an electron beam of 5 keV with a current of 10 000 nA. The considered electron flux was 3e13 electrons cm^{-2} s^{-1}.

The estimated experimental desorption yield for the experiments were considered to 2e-2 molecules/electron (Meier & Loeffler, 2020). Following Mifsud et al. (2022b), the penetration depth of 5 keV electrons in such ices is ~0.2 μm indicating that the samples were fully illuminated. The illuminated sample area was roughly 1.8 cm^2. Finally, for H_2O, an initial column density of 3.6e17 molecules cm^{-2} was considered, followed by a linear decrease until the estimated final column density (around 96.5 per cent of the initial value).

The data set itself consists of a set of 20–25 pairs of points containing the molecular abundances, in units of column density, of the observed species with their respective irradiation times. To increase the accuracy of the model, for each observed species, it were considered 2800 not-equally spaced interpolated data points ranging from 0 to 5000 s (~1.4 h). It is important to note that no structure was added or omitted from the modeled data during the interpolation process.

In the experimental work of Zheng et al. (2006), the authors observed that the production rates of H_2, O_2, and H_2O_2 decreased as the temperature increased from 12 to 90 K. This suggests that a thermal, possibly diffusion-controlled component of the reaction mechanism is present. This component could facilitate the back-reaction of the primarily formed irradiation products, such as the recombination of atomic H with OH to regenerate water. Based on this assumption, we develop a reaction network that considers 61 coupled equations, describing the chemical evolution and abundances of selected molecules in crystalline water ices in the presence of incoming 5 keV electrons. The network consists of several radiation-induced dissociation reactions, bimolecular collision reactions, and radiation-induced desorption reactions. Here, we considered nine different chemical species within the ice, including five observed species [H_2, H_2O, O_2, H_2O_2, and O_3 (this assumed to be an ‘observed’ species with a virtually negligible column density for calculation purposes)] and four non-observed but predicted species (H, O, OH, and HO_2). The proposed reaction network will be described in detail below.

2.2. Brief PROCODA description

The PROCODA code detailed in Pilling et al. (2022) solves a system of coupled differential equations to describe the chemical evolution of typical astrophysical ices, as a function of time, during the processing by ionizing radiation (see also Carvalho et al. 2022). The code also employs a set of thermochemistry data for the modeled species, used in the first stage of calculations to rank the ERCs, as explained in detail in Pilling et al. (2023) and Pilling et al. (in preparation).

Briefly, the typical equation in the chemically coupled system solved by the code has the following parameters:

$$\frac{\mathrm{d}N_i}{\mathrm{d}t} = \left[-DES_i\,(t) - \sum_{d1} k_{d1} N_i\,(t) - \sum_{d2} k_{d2} N_i\,(t)\,N_a\,(t) \right] + \left[\sum_{p1} k_{p1} N_a\,(t) + \sum_{p2} k_{p2} N_a\,(t)\,N_b\,(t) \right] \left[\text{molecules cm}^{-2}\ \text{s}^{-1}\right], \quad (1)$$

where dN_i/dt is the column density (or concentration) variation along the time t of a given species i, and the k values are the ERCs for the different reactions. The values k_{d1} and k_{d2} indicate the destruction (consumption) processes, and values k_{p1} and k_{p2} indicate the production processes of a given species i, in direct and bimolecular reactions. In this equation, the $DES_i(t) = k_{des,i}\ \Omega_\mathrm{i}\ (t)\ N_i(t)$ is the differential column density desorption, i.e. the number of molecules (or atomic species) that desorbs from ice to gas-phase per cm^2 and per second due to incoming radiation, which also depends on the intrinsic desorption rate ($k_{des,i}$), in units of s^{-1}, and the dimensionless surface coverage of the species i as a function of time ($\Omega_\mathrm{i}\ (t)$). The values N_a *and* N_b indicate the column densities (or concentrations) of species a and b, respectively, which participate in the reaction to produce or consume the respective i species. The list with the full employed equations is presented in Appendix A.

Fig. 1 presents a scheme with selected reactions considered in this work to map the evolution of crystalline water ice under bombardment by fast electrons. Species highlighted in the gray boxes are commonly detected by FTIR experiments. As discussed before, O_3 was not detected in current experimental data (it was considered an ‘observed’ species once with a very low column density, below the detection spectrometer detection limit).

The code details, including the employed equations, the coupled equation minimization algorithm (L_BFGS-B algorithm), its explanatory flowchart, input/output parameters, and the convergence criteria, are fully explained in Pilling et al. (2022; 2023). Briefly, to solve the coupled chemical equation set, the code employs a minimization process of a score function (SF) that evaluates how close the system is to its minimum global solution. The SF employed in the minimization algorithm during the search for the best solution of coupled chemical systems and a discussion of the employed parameters are presented in Appendix B.

As described by Pilling et al. (2022), the code performs several calculation loops during a typical run until the best-fitting solution is found (the one with the lowest summed chi-square function, χ^2). This iterative process incorporates the ERCs obtained from the previous best-fitting calculation as inputs for the subsequent calculations, thus ensuring that the ordering hypothesis is continually refined and improved with each iteration.

2.3 Thermochemistry data

The ERCs ordering hypothesis is a procedure that uses thermochemistry data to rank ERCs (exothermic reaction complexes) by reaction enthalpy. Exothermic reactions are prioritized due to their higher probability of occurring, which helps to reduce solution degeneracy and provide more accurate predictions of ERCs abundances in astrophysical environments. Additionally, the thermochemical data used in the ordering hypothesis for the ERCs, considers that all studied species are at the lowest energy level, and formation enthalpies and reaction enthalpies are in the gas-phase at the theoretical temperature of 0 K. Additional details of the ordering procedure are given in Pilling et al. (2023) and Pilling et al. (in preparation).

The list of the chemical species and gas-phase formation enthalpies at 0 K ($\boldsymbol{\Delta_f H^0}$) considered in this work is presented in Table 1. These species were chosen since they present the lowest formation enthalpies (a criterion employed in the enthalpy reaction calculation). The reaction enthalpies employed in the ordering hypothesis for the ERCs were calculated from these listed formation enthalpies, as we discuss further.

2.4 Advantages and limitations of the PROCODA code

The PROCODA code is an effective tool for determining the ERCs of chemical reactions in astrophysical ices. It uses a system of coupled chemical equations to calculate rate constants from experimental data. The code assumes that the overall reaction orders are determined by the sum of the number of reactants in each reaction, and that all desorption reactions are first-order reactions. This approach provides a more accurate and reliable determination of reaction kinetics and rate constants than other methodologies, which assume a first-type order or pseudo-first order for all reactions (e.g. Jamieson et al. 2006; Bennett et al. 2009, 2010; Bossa et al. 2015).

It is worth noting that due to the constant exposure to radiation, astrophysical ices are able to overcome the activation barriers of most reactions through the absorption of incoming energy, as well as the distribution of energy within the ice by the secondary electrons. The incoming energy is redistributed within the ice, mainly due to the collision with uncountable secondary electrons. Therefore, as a limitation, it can be mentioned that some of the physicochemical processes and quantities presented in this manuscript may not have obvious explanations when compared to the studied single reactions in the solid or gas-phase.

Another limitation is that the code is limited by the number of species and chemical reactions that can be included in the model, and it does not explicitly consider ionic and excited species.

However, despite these limitations, the PROCODA code can provide valuable information on the kinetics and abundances of chemical species in H_2O-rich astrophysical ices that undergo processing by ionizing radiation, as well as information on radiation-induced desorption processes. For a more comprehensive discussion of the code’s advantages, uncertainties, and limitations, see Pilling et al. (2022, 2023).

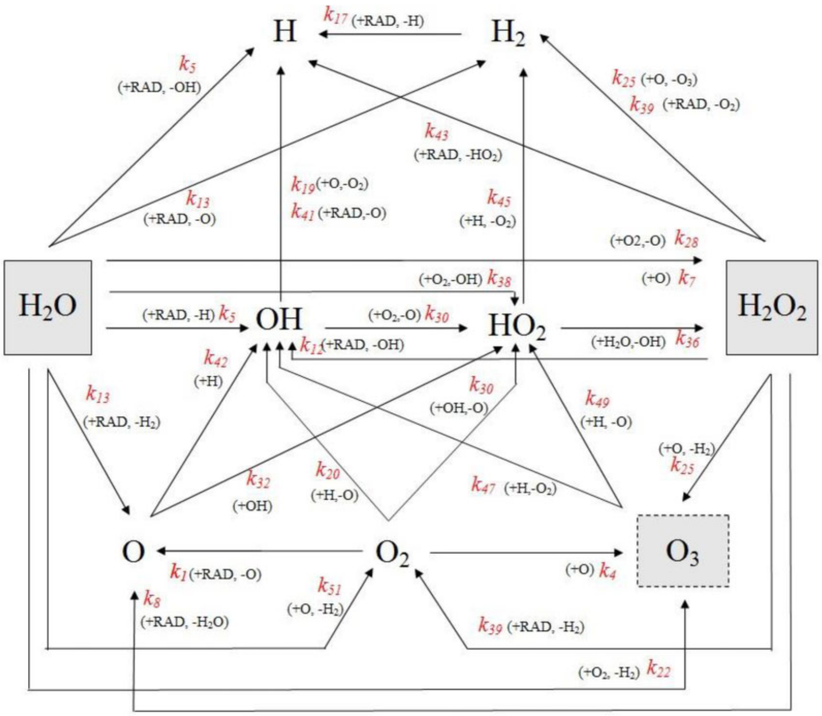

Figure 1. Schematics of some selected reactions in the studied chemical network. Species highlighted in the gray boxes are commonly detected by FTIR experiments (see the full reaction set at Table 2). O_3 was not detected in current experimental data, and its column density was considered very low (below the detection limit) for numerical calculation purposes. See details in the text.

Table 1. Chemical species and gas-phase formation enthalpies at 0 K ($\Delta_f H^0$) considered in this work.

Species (additional info)	$\Delta_f H^0$ (kJ mol^{-1})	Ref. and notes.
H (atomic hydrogen)	216.03	[1]
H_2 (molecular hidrogen)	0	[1]
O (atomic oxygen; triplet)	246.8	[1]
OH (hydroxil radical)	37,11	[2]
H_2O (water)	−238.9	[2]
O_2 (molecular oxygen, triplet)	0	[1]
HO_2 (hydroperoxyl radical)	15.23	[2]
H_2O_2 (hydrogen peroxide)	−129.74	[2]
O_3 (ozone)	144.4	[1]

[1] Obtained from the Active Thermochemical Tables version 1.122p at https://atct.anl.gov/ (see also Ruscic et al. 2004; Ruscic et al. 2005; Ruscic & Bross 2020); [2] obtained from https://cccbdb.nist.gov/ considering experimental data.

3 RESULTS AND DISCUSSION

The results of this investigation were divided into four sections: the first to present the best-fitting models obtained and their comparison; the second to present the effect of temperature on the ERCs; a third section to make a comparison between the employment of PROCODA in crystalline and amorphous water ices; and a final section about the CE at different temperatures obtained after large exposure to 5 keV electrons.

3.1 Best-fitting models

Fig. 2 shows the evolution of column density for the most accurate models generated with the PROCODA code on pure crystalline H_2O ices irradiated by 5 keV electrons at four different temperatures: 12, 40, 60, and 90 K. The experimental data were taken from Zheng et al. (2006) and are displayed by the black symbols in the figure. We modeled nine species, five of which were observed in the experiment work (H_2, H_2O, O_2, H_2O_2, O_3) and four were predicted but not observed (H, O, OH, HO_2). As discussed before, O_3 was not strictly measured in the experimental data, but it was considered as an observed species with a very low value (below the spectrometer limit for numerical calculation purposes). The dashed line represents the summed column density for the desorbed species. The figure header displays some model parameters, including the SF, the chi-squared function (χ^2), the desorption yield (Y), the mass similarity criterion (MSC), and the slope similarity criterion (SSC). The obtained values for χ^2 were 5.44, 4.09, 2.08, and 0.13, for the models at temperatures at 12, 40, 60, and 90 K, respectively.

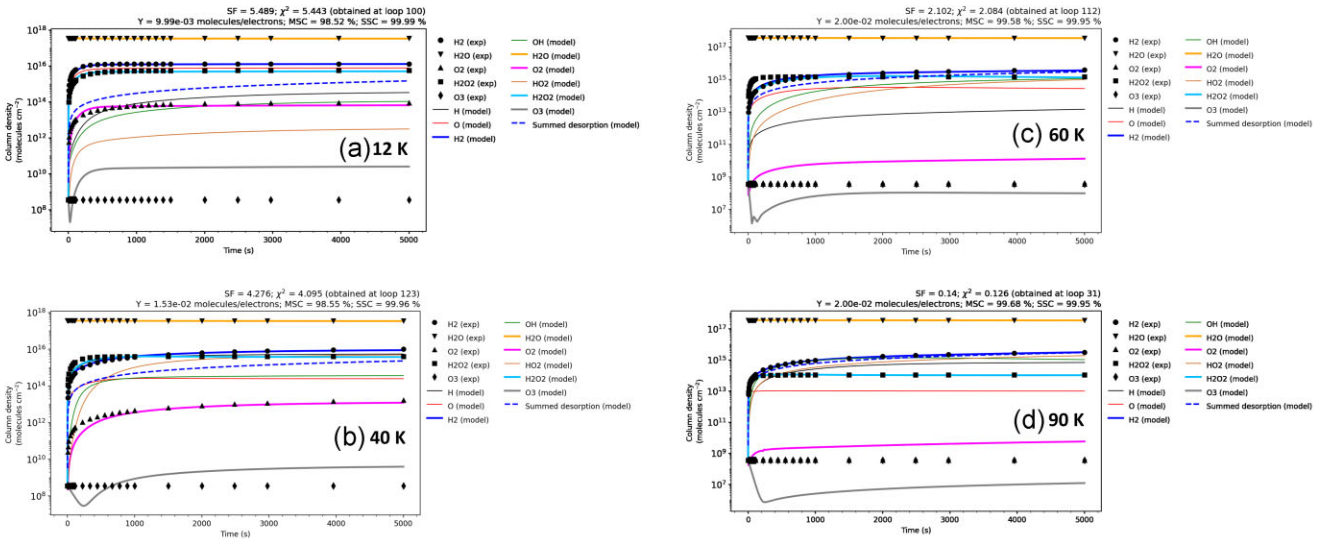

Figure 2. The evolution of column density obtained for the best-fitting model employing the PROCODA on crystalline H_2O ices irradiated by 5 keV electrons at different temperatures (data from Zheng et al. 2006). (a), (b), (c), and (d) present the best-fitting models for the data at the temperatures of 12, 40, 60, and 90 K. The black symbols represent the experimental data. The bold-dashed blue line represents the modeled summed desorption column density. O_3 was not detected in current experimental data, and its abundance was considered very low (below the detection limit) for numerical calculation purposes. Important model output parameters are displayed in the header. See details in the text.

From Fig. 2 we notice that the models presented a very good match with the experimental data. Some deviation is observed for the modeling of O_3 data and in the case of 90 K also for O_2. The modeled Y presents a slight increase as a function of the temperature of ice which ranges from 1–2e-2 molecules/electrons. The discussion on the abundances at the CE phase reached at large radiation fluences will be presented later.

3.2 ERCs at different ice temperatures

Table 2 lists the reactions employed and the calculated ERCs (k values) obtained for the best-fitting models employing the PROCODA code on pure crystalline H_2O ices irradiated by 5 keV electrons at four different temperatures (data from Zheng et al. 2006). The listed values also include the branching ratio [BR (per cent)] for the considered reactions within reaction groups. The reaction enthalpies at gas-phase at 0 K ($\Delta_r H$), also presented in Table 2, employed in the ordering hypothesis for the ERCs, were calculated by the difference between the sum of the formation enthalpies of products and the sum of formation enthalpies of reactants in each reaction (see values at Table 1). The $\Delta_r H$ were calculated considering the lowest formation enthalpy for each species. The parameter k label indicates if the reaction is within a group or not or if is a radiation induced desorption.

It is noteworthy that some reactions considered in the model are endothermic (in the gas-phase), and might not be able to occur at low temperatures. However, due to the constant energy input by the incoming projectiles, these reactions have the possibility of occurring. The error in rate constants was estimated to be below 20 per cent as discussed by Pilling et al. (2022).

Table 2 highlights the temperature dependence of the branching ratios of certain reactions. This dependence can be attributed to the effects of temperature on the mobility of species and the density of the ice, which can also influence the distribution of electron energy through the ice. Moreover, at higher temperatures, the electrons, particularly those with low energy, can diffuse more freely throughout the ice's lattice, increasing the likelihood of interacting with molecules and leading to higher reaction probabilities. For several reactions, the BR increases with the temperature, as in the case of $H + OH \rightarrow H_2O$ (indicated by k6), $H_2O_2 + RAD \rightarrow OH + OH$ (indicated by k12), $H_2 + O \rightarrow H + OH$ (indicated by k15), $H_2O + O_2 \rightarrow OH + HO_2$ (indicated by k38), $H + O_3 \rightarrow O + HO_2$ (indicated by k19), and others. However, for other reactions, curiously, the BR is very enhanced at low temperatures, for example, the case of $H + O + OH \rightarrow H + O_2$ (indicated by k19), $HO_2 + RAD \rightarrow H + O_2$ (indicated by k33), $HO_2 \rightarrow H_2 + O_2$ (indicated by k45), and $OH + O_2 \rightarrow H + O_3$ (indicated by k45). Future investigations should go deeper into this finding to explain such effect and how this is related with the ices' physicochemical parameters.

Fig. 3 presents a bar plot with the values of the radiation-induced intrinsic desorption rate constant calculated by the models for different ice temperatures. As an overall tendency, we observe that as the ice temperature increases, the intrinsic desorption rate constants also increase, which is the strict behavior of H and H_2O (indicated by k53 and k57, respectively). For H_2O_2 (indicated by k60) the maximum occurs at 60 K. Curiously, for some species (e.g. O, H_2, OH, and HO_2, indicated by k54, k56, k59, and k60, respectively), the lowest value for this parameter was observed for the ice at 40 K.

A bar plot with the values of the radiation-induced dissociation rate constant calculated by the models for different ice temperatures is presented in Fig. 4. For several reactions, we observe a decreasing of ERCs as a function of temperature (e.g. k1, k3, k8, k13, k31, k33, k39, k41). This is true, for example, for the dissociation reaction of H_2O yielding $H_2 + O$ (indicated by k13) but is not for the route yielding $H + OH$ (indicated by k5) which does not present any clear dependence with the temperature.

The increasing radiation-induced dissociation rate constant as a function of temperature was observed for some reactions (e.g. k12,

Table 2. Reactions considered in the model to map the chemical evolution of crystalline H_2O ice irradiated by 5 keV electrons at different temperatures (data from Zheng et al. 2006) and the main outcomes from the best-fitting models, including the ERCs (k values) and the branching ratio [BR(per cent)] of reactions within the considered reaction groups.

Reactions parameters						12 K		40K		60K		90K	
Reaction label	Reactants	Products	$\Delta_r H$	k label*	k unit	k value	BR(per cent)	k value	BR(per cent)	k value	BR(per cent)	k value	BR(per cent)
r1	O2 + RAD	O + O	493.68	k1 (single; most endothermic within the direct dissociation reactons)	s^{-1}	1.72e-01	100.00	9.45e-02	100.00	7.14e-02	100.00	7.49e-02	100.00
r2	O + O	O2	− 493.68	k2 (single)	cm^3 molecules^{-1} s^{-1}	3.57e-24	100.00	5.93e-25	100.00	2.42e-29	100.00	7.64e-26	100.00
r3	O3 + RAD	O + O2	102.45	k3 (single)	s^{-1}	1.46e-01	100.00	1.30e-02	100.00	8.84e-02	100.00	3.28e-02	100.00
r4	O + O2	O3	− 102.45	k4 (single)	cm^3 molecules^{-1} s^{-1}	8.38e-26	100.00	5.07e-26	100.00	4.34e-27	100.00	1.60e-25	100.00
r5	H2O + RAD	H + OH	492.04	k5 (G9; [13, k5])	s^{-1}	1.00e-08	0.01	1.00e-08	0.04	1.00e-08	0.17	1.00e-08	0.37
r6	H + OH	H2O	− 492.04	k6 (G4; [K6, k16])	cm^3 molecules^{-1} s^{-1}	3.20e-24	49.54	9.80e-24	55.75	4.44e-26	88.43	4.79e-24	99.83
r7	O + H2O	H2O2	− 137.68	k7 (G12; [k7, k51])	cm^3 molecules^{-1} s^{-1}	5.17e-24	100.00	2.63e-23	100.00	9.76e-24	100.00	3.44e-24	100.00
r8	H2O2 + RAD	O + H2O	137.68	k8 (G10; [k39, k8, k12, k43])	s^{-1}	2.38e-01	100.00	4.84e-02	100.00	6.15e-02	99.80	1.48e-03	15.86
r9	OH + H2O	H2O2 + H	288.08	k9 (single; most endothermic within the bimolecular reactons)	cm^3 molecules^{-1} s^{-1}	1.19e-24	100.00	1.23e-25	100.00	8.07e-27	100.00	2.64e-28	100.00
r10	H + H2O2	OH + H2O	− 288.08	k10 (single)	cm^3 molecules^{-1} s^{-1}	3.76e-24	100.00	5.46e-24	100.00	8.82e-25	100.00	5.92e-24	100.00
r11	OH + OH	H2O2	− 203.96	k11 (single)	cm^3 molecules^{-1} s^{-1}	3.85e-24	100.00	2.82e-24	100.00	4.68e-25	100.00	4.60e-27	100.00
r12	H2O2 + RAD	OH + OH	203.96	k12 (G10; [K39, k8, k12, k43])	s^{-1}	1.00e-08	0.00	1.00e-08	0.00	6.98e-05	0.11	4.77e-03	51.11
r13	H2O + RAD	H2 + O	485.74	k13 (G9; [k13, k5])	s^{-1}	1.40e-04	99.99	2.27e-05	99.96	5.84e-06	99.83	2.67e-06	99.63
r14	H2 + O	H2O	− 485.74	k14 (G5; [k14, k15])	cm^3 molecules^{-1} s^{-1}	5.96e-24	100.00	2.69e-23	98.93	2.53e-23	99.97	1.33e-23	85.48
r15	H2 + O	H + OH	6.3	k15 (G5; [K14, k15])	cm^3 molecules^{-1} s^{-1}	9.93e-29	0.00	2.90e-25	1.07	8.20e-27	0.03	2.26e-24	14.52
r16	H + OH	H2 + O	− 6.3	k16 (G4; [k6, k16])	cm^3 molecules^{-1} s^{-1}	3.26e-24	50.46	7.78e-24	44.25	5.81e-27	11.57	8.30e-27	0.17
r17	H2 + RAD	H + H	432.06	k17 (single)	s^{-1}	1.00e-08	100.00	8.04e-03	100.00	2.64e-05	100.00	1.88e-05	100.00
r18	H + H	H2	− 432.06	k18 (single)	cm^3 molecules^{-1} s^{-1}	4.26e-24	100.00	2.57e-23	100.00	3.34e-26	100.00	1.10e-23	100.00
r19	O + OH	H + O2	− 67.92	k19 (G15; [k32, k19])	cm^3 molecules^{-1} s^{-1}	2.15e-24	89.77	2.97e-26	2.40	1.18e-28	0.03	2.55e-28	0.00
r20	H + O2	O + OH	67.92	k20 (G2; [k34, k20])	cm^3 molecules^{-1} s^{-1}	2.40e-25	64.34	6.39e-27	9.52	9.13e-26	22.14	4.58e-26	46.03
r21	H + H2O	H2 + OH	59.98	k21 (single)	cm^3 molecules^{-1} s^{-1}	8.10e-25	100.00	3.19e-31	100.00	2.09e-24	100.00	3.51e-26	100.00
r22	H2 + OH	H + H2O	− 59.98	k22 (single)	cm^3 molecules^{-1} s^{-1}	5.61e-24	100.00	1.44e-24	100.00	1.07e-24	100.00	5.41e-24	100.00
r23	H2O + O2	H2 + O3	383.29	k23 (G8; [k38, k28, k23])	cm^3 molecules^{-1} s^{-1}	3.19e-31	0.00	3.19e-31	0.00	1.49e-27	0.01	8.60e-29	0.00
r24	H2 + O3	O2 + H2O	− 383.29	k24 (G7; [k24, k26])	cm^3 molecules^{-1} s^{-1}	2.58e-24	48.59	9.20e-27	4.16	1.03e-24	53.12	1.07e-25	59.78
r25	O + H2O2	H2 + O3	27.29	k25 (G13; [k27, k25])	cm^3 molecules^{-1} s^{-1}	3.19e-31	0.00	3.20e-30	0.00	1.76e-28	38.77	9.79e-29	0.75
r26	H2 + O3	O + H2O2	− 27.29	k26 (G7; [k24, k26])	cm^3 molecules^{-1} s^{-1}	2.73e-24	51.41	2.12e-25	95.84	9.09e-25	46.88	7.20e-26	40.22
r27	O + H2O2	H2O + O2	− 356	k27 (G13; [k27, k25])	cm^3 molecules^{-1} s^{-1}	2.27e-24	100.00	5.23e-24	100.00	2.78e-28	61.23	1.30e-26	99.25
r28	H2O + O2	O + H2O2	356	k28 (G8; [k38, k28, k23])	cm^3 molecules^{-1} s^{-1}	7.85e-24	99.49	3.34e-24	61.17	1.21e-23	71.89	1.41e-24	37.90
r29	O + HO2	OH + O2	− 224.96	k29 (G14; [k29, k50])	cm^3 molecules^{-1} s^{-1}	2.76e-24	100.00	5.54e-27	99.78	1.33e-28	54.51	4.82e-28	67.79
r30	OH + O2	O + HO2	224.96	k30 (G16; [k30, k48])	cm^3 molecules^{-1} s^{-1}	1.78e-25	66.62	2.16e-27	2.11	1.18e-25	95.34	1.04e-25	99.83
r31	HO2 + RAD	O + OH	268.72	k31 (G11; [k33, k31])	s^{-1}	7.65e-02	83.70	1.19e-05	4.02	7.38e-05	94.34	5.69e-06	93.36
r32	O + OH	HO2	− 268.72	k32 (G15; [k32, k19])	cm^3 molecules^{-1} s^{-1}	2.45e-25	10.23	1.21e-24	97.60	4.11e-25	99.97	8.03e-24	100.00
r33	HO2 + RAD	H + O2	200.8	k33 (G11; [k33, k31])	s^{-1}	1.49e-02	16.30	2.84e-04	95.98	4.43e-06	5.66	4.05e-07	6.64
r34	H + O2	HO2	− 200.8	k34 (G2; [k34, k20])	cm^3 molecules^{-1} s^{-1}	1.33e-25	35.66	6.07e-26	90.48	3.21e-25	77.86	5.37e-26	53.97
r35	OH + H2O2	H2O + HO2	− 131.04	k35 (single)	cm^3 molecules^{-1} s^{-1}	7.10e-24	100.00	2.51e-23	100.00	2.82e-24	100.00	5.94e-24	100.00
r36	H2O + HO2	OH + H2O2	131.04	k36 (single)	cm^3 molecules^{-1} s^{-1}	1.55e-24	100.00	3.79e-28	100.00	4.55e-27	100.00	1.78e-28	100.00
r37	OH + HO2	H2O + O2	− 291.24	k37 (single)	cm^3 molecules^{-1} s^{-1}	2.08e-24	100.00	7.35e-25	100.00	4.43e-29	100.00	2.78e-29	100.00
r38	H2O + O2	OH + HO2	291.24	k38 (G8; [k38, k28, k23])	cm^3 molecules^{-1} s^{-1}	3.99e-26	0.51	2.12e-24	38.83	4.73e-24	28.10	2.31e-24	62.10
r39	H2O2 + RAD	H2 + O2	129.74	k39 (G10; [k39, k8, k12, k43])	s^{-1}	1.09e-05	0.00	1.00e-08	0.00	2.19e-06	0.00	2.63e-06	0.03

Table 2 – *continued*

Reactions parameters Reaction label	Reactants	Products	$\Delta_r H$	k label*	k unit	12 K k value	12 K BR(per cent)	40K k value	40K BR(per cent)	60K k value	60K BR(per cent)	90K k value	90K BR(per cent)
r40	H2 + O2	H2O2	− 129.74	k40 (G6; [k40, k52, k46])	cm^3 molecules^{-1} s^{-1}	1.15e-23	70.86	1.40e-23	56.47	1.02e-24	27.35	4.24e-25	74.31
r41	OH + RAD	H + O	425.76	k41 (single)	s^{-1}	4.91e-02	100.00	8.06e-03	100.00	1.02e-05	100.00	1.56e-06	100.00
r42	H + O	OH	− 425.76	k42 (single)	cm^3 molecules^{-1} s^{-1}	5.34e-24	100.00	1.17e-24	100.00	2.79e-25	100.00	2.94e-24	100.00
r43	H2O2 + RAD	H + HO2	361	k43 (G10; [39, k8, k12, k43])	s^{-1}	1.00e-08	0.00	1.00e-08	0.00	4.90e-05	0.08	3.08e-03	33.00
r44	H + HO2	H2O2	− 361	k44 (G1; [k44, k45])	cm^3 molecules^{-1} s^{-1}	6.06e-25	34.51	1.88e-25	23.80	1.72e-26	99.25	8.80e-28	95.69
r45	H + HO2	H2 + O2	− 231.26	k45 (G1; [k44, k45])	cm^3 molecules^{-1} s^{-1}	1.15e-24	65.49	6.02e-25	76.20	1.30e-28	0.75	3.96e-29	4.31
r46	H2 + O2	H + HO2	231.26	k46 (G6; [k40, k52, k46])	cm^3 molecules^{-1} s^{-1}	2.07e-28	0.00	9.40e-26	0.38	1.32e-24	35.39	8.98e-26	15.74
r47	H + O3	OH + O2	− 323.31	k47 (G3; [k47, k49])	cm^3 molecules^{-1} s^{-1}	2.12e-24	95.02	8.46e-26	20.45	2.40e-25	46.69	4.19e-28	6.18
r48	OH + O2	H + O3	323.31	k48 (G16; [k30, k48])	cm^3 molecules^{-1} s^{-1}	8.92e-26	33.38	1.00e-25	97.89	5.77e-27	4.66	1.77e-28	0.17
r49	H + O3	O + HO2	− 98.35	k49 (G3; [k47, k49])	cm^3 molecules^{-1} s^{-1}	1.11e-25	4.98	3.29e-25	79.55	2.74e-25	53.31	6.36e-27	93.82
r50	O + HO2	H + O3	98.35	k50 (G14; [k29, k50])	cm^3 molecules^{-1} s^{-1}	1.16e-30	0.00	1.21e-29	0.22	1.11e-28	45.49	2.29e-28	32.21
r51	O + H2O	H2 + O2	− 7.94	k51 (G12; [k7, k51])	cm^3 molecules^{-1} s^{-1}	1.53e-28	0.00	3.19e-31	0.00	6.07e-29	0.00	8.43e-29	0.00
r52	H2 + O2	O + H2O	7.94	k52 (G6; [k40, k52, k46])	cm^3 molecules^{-1} s^{-1}	4.73e-24	29.14	1.07e-23	43.16	1.39e-24	37.27	5.68e-26	9.95
r53	H desorption	-	NA	k53 (desorption)	s^{-1}	7.05e-07	100.00	8.83e-07	100.00	2.62e-06	100.00	5.66e-06	100.00
r54	O desorption	-	NA	k54 (desorption)	s^{-1}	1.90e-06	100.00	1.57e-07	100.00	3.49e-06	100.00	1.95e-06	100.00
r55	H2 desorption	-	NA	k55 (desorption)	s^{-1}	1.69e-06	100.00	9.06e-07	100.00	7.38e-06	100.00	3.07e-06	100.00
r56	OH desorption	-	NA	k56 (desorption)	s^{-1}	2.07e-06	100.00	1.40e-07	100.00	6.12e-06	100.00	5.15e-06	100.00
r57	H2O desorption	-	NA	k57 (desorption)	s^{-1}	9.37e-07	100.00	1.40e-06	100.00	1.72e-06	100.00	1.71e-06	100.00
r58	O2 desorption	-	NA	k58 (desorption)	s^{-1}	6.78e-07	100.00	1.11e-06	100.00	2.08e-06	100.00	1.00e-06	100.00
r59	HO2 desorption	-	NA	k59 (desorption)	s^{-1}	1.99e-06	100.00	2.85e-07	100.00	6.87e-06	100.00	2.17e-06	100.00
r60	H2O2 desorption	-	NA	k60 (desorption)	s^{-1}	2.21e-06	100.00	2.44e-07	100.00	3.35e-06	100.00	1.53e-06	100.00
r61	O3 desorption	-	NA	k61 (desorption)	s^{-1}	5.19e-07	100.00	8.11e-07	100.00	6.39e-06	100.00	1.08e-06	100.00

*single reaction: (single); reaction within groups: [Group label; (Group members ranked by thermochemistry only with the most exothermic first)]; intrinsic desorption: (desorption).

NA: Not applied. See details and explanations in the text.

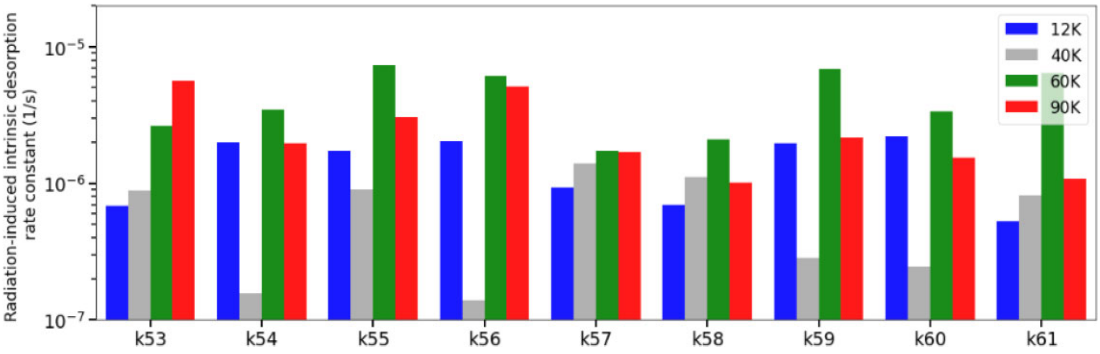

Figure 3. Radiation-induced intrinsic desorption rate constant at different ice temperatures.

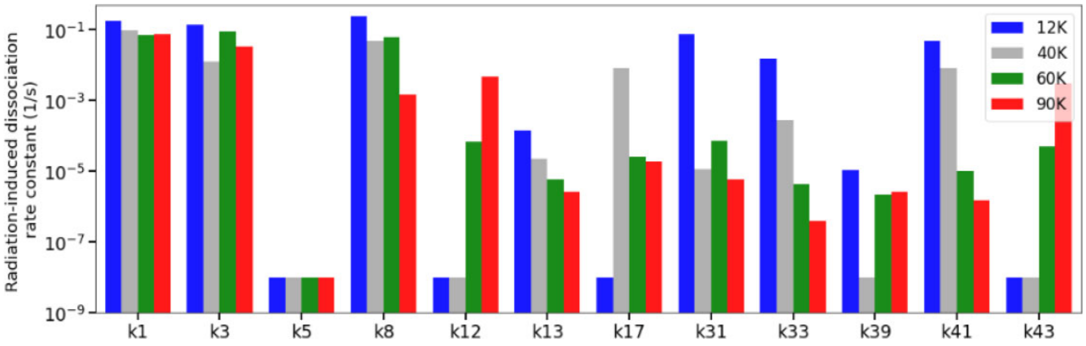

Figure 4. Radiation-induced dissociation rate constant at different ice temperatures.

k17, k43). Curiously, two of them were the dissociative reactions driven by radiation on the H_2O_2 yielding OH + OH (indicated by k12) and H + HO_2 (indicated by k43).

Fig. 5 displays a bar graph of the radiation-induced bimolecular rate constants calculated by the models for various ice temperatures. Panel (a) presents the ERCs from k2 up to k27, and panel (b) from k28 up to k52. Here, once again, the dependence of the temperature on the ERC depends on the type of reaction. For example, most bimolecular reactions have a clear decreasing of ERCs as temperature increases, as in the case of reactions indicated by k2, k9, k11, k19, k29, k36, k37, k40, k42, k44, k45, k47, k84, and k52. However, for some reaction we observe a contrary behavior (e.g. k23, k25 k32, k38, and k50)

The relationship between reaction rates and temperature in ices exposed to ionizing radiation, like those studied in this work, may vary depending on the specific reaction mechanism. Generally, reactions that require thermal energy to proceed, such as diffusion-limited reactions, will have reaction rates that increase with temperature, as there is more thermal energy available to activate these reactions. On the other hand, reactions that are barrier-limited, meaning that they require an activation energy barrier to be overcome, will have reaction rates that decrease with temperature, as the thermal energy available at lower temperatures may not be sufficient to overcome the activation energy barrier.

Moreover, it is important to note that the effect of temperature on reaction rates can be complicated by the fact that temperature also affects the structure and morphology of the ice. At higher temperatures, the ice may undergo structural changes that can affect reaction rates, such as increasing or decreasing the number of active sites available for reactions. Additionally, the mobility of molecules in the ice may change with temperature, affecting the likelihood of reactants coming into contact with one another. Therefore, the complex interplay between temperature, reaction mechanism, and ice structure/morphology can lead to varying dependencies of reaction rates on temperature in irradiated astrophysical crystalline water ice.

To facilitate a more comprehensive comparison of the models generated for crystalline water ice at varying temperatures, we have depicted three bar graphs in Fig. 6. These graphs exhibit the mean values of ERCs for radiation-induced intrinsic desorption (panel a), dissociation (panel b), and bimolecular reactions (panel c), respectively. Our observations indicate that warm crystalline water ices exhibits higher average radiative-induced intrinsic desorption compared to colder ices. Moreover, as the temperature increases, we note a corresponding decrease in the average ERC values for radiation-induced dissociation and bimolecular collisions. This behavior might be associated with the decrease in density of the ice as it heats. At higher temperatures, the molecules in the ice have more thermal energy and are thus more mobile, leading to an increase in the average distance between molecules. As the distance between molecules increases, the probability of a molecule being hit by a photon decreases, resulting in a decrease in the rate of radiation-induced dissociation process. Additionally, at higher temperatures, there may be more thermally induced structural defects in the ice, which can serve as sites for reactions to occur. However, these defects may also lead to the formation of more stable products that inhibit further reactions from occurring. As a result, the overall rate of radiation-induced dissociation may decrease at higher temperatures due to a combination of these factors.

Curiously, the ice at 40 K presented a larger average value of ERC for bimolecular collisions, which might be attributed to the increased mobility of specific species at this temperature, allowing for more frequent collisions. Additionally, it is possible that at the higher temperature of 40 K, the molecules in the ice are more ordered than at 12 K, resulting in a more favorable orientation for collisions

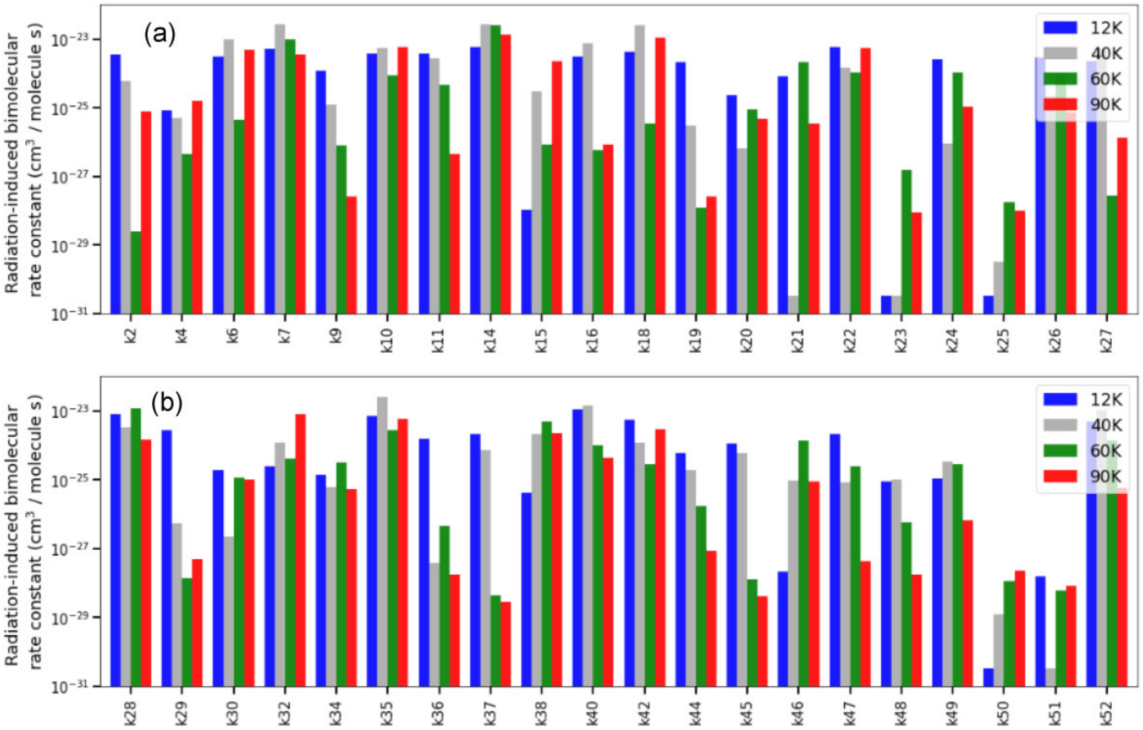

Figure 5. Radiation-induced bimolecular rate constant at different ice temperatures.

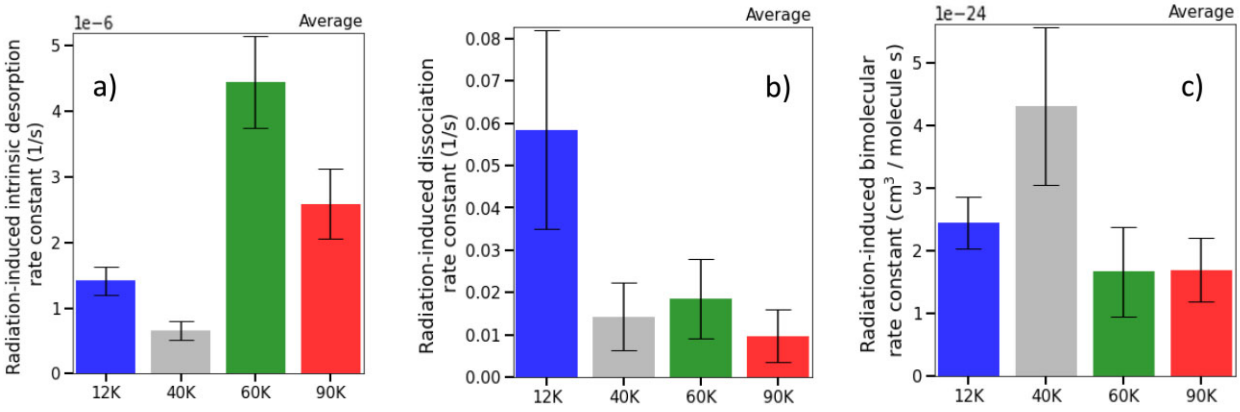

Figure 6. Average values for ERCs for radiation-induced intrinsic desorption (panel a), dissociation (panel b), and bimolecular reactions (panel c) for the different ice temperatures.

to occur. However, further investigation is necessary to confirm this hypothesis and clarify this issue.

Fig. 7 presents the calculated radiation-induced desorption rate and yield for the studied crystalline water ices. The ERCs for the desorption reactions increase as the temperature of crystalline water ice, under bombardment by fast electrons, increases due to the increased mobility of molecules in the ice. With the enhancement of ice's temperature, the thermal energy of the molecules increases, eventually increasing the average distance between molecules. This increased distance allows for more free volume in the ice and thus a higher probability of molecules reaching the surface of the ice where they can be desorbed by incoming electrons. Additionally, at higher temperatures, there may be more thermally induced structural defects in the ice, which can serve as sites for desorption to occur. Furthermore, the desorption energy barrier for a particular species may decrease with increasing temperature, making it easier for the species to overcome the barrier and desorb from the ice. As a result, the overall rate of radiation-induced desorption increases at higher temperatures due to a combination of these factors.

As pointed out by Zheng et al. (2006), the diffusion coefficient of atomic (e.g. oxygen, hydrogen) and radical (OH) species is highly sensitive to temperature enhancement (see also Hori & Hondoh 2003) which may also help to explain the enhancement of the average desorption rate with temperature. We will discuss more about desorption at the CE phase in Section 4.

3.3 Comparison between crystalline and amorphous water ices

Recently, Da Silveira & Pilling (in preparation) have employed the PROCODA code to map the chemical evolution of amorphous H_2O ice at very low temperatures irradiated with different ionizing radiations

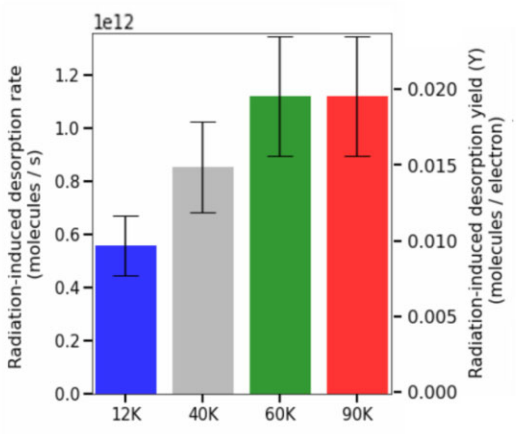

Figure 7. Radiation-induced desorption rate (left y-axis) and yield (right y-axis) for the different ice temperatures.

such as a cosmic ray analogue, UV, broad-band X-rays, and 2 keV electrons. The authors quantified the ERCs and the branching ratio of several chemical reactions and observed that the average values obtained with UV were close to the ones obtained with 2 keV electrons (experimental data taken from Mifsud et al. 2022b).

A comparison between the average parameters of the best-fitting models for 2 keV electron bombardment amorphous H_2O ice at 20 K (Da Silveira & Pilling, in preparation) with the 5 keV electron bombardment crystalline H_2O ice at 12 K (this work) is presented in Table 3. The current investigation indicates that crystalline ice has a lower value of ERCs for both radiation-induced dissociation and bimolecular reactions compared to amorphous ice. The ERCs for the intrinsic desorption reactions in both ices were close, with a slight enhancement in the case of crystalline ice. The largest difference was observed in molecular desorption. The desorption rate in crystalline ice was approximately five times larger than the calculated value for the amorphous sample. Furthermore, the desorption yield (Y) in crystalline ice was approximately 1e-2 molecules electrons^{-1}, which was significantly higher than the value of 3.2e-4 molecules electrons^{-1} obtained for the amorphous sample.

Curiously, Martinez et al. (2019) observed the opposite behavior when comparing the desorption of amorphous and crystalline water ices in experiments employing 90 keV O ions as a projectile. The authors, have irradiated water ice targets at several temperatures (10–200 K) and used time-of-flight mass spectrometry (TOF-SIMS) to analyse the sputtering of secondary ions that occurred after bombarding an ice target. In their investigation, the authors suggest that the ionic sputtering yield for crystalline water ice is much lower than for amorphous ices. Additionally, they also pointed out that their findings corroborate the relationship between sputtering yields of ionic species and the structure of water ice (amorphous ices present larger sputtering yields than crystalline ices deposited at high temperatures or deposited at low temperatures and subsequently heated to ∼150 K). This effect has not been previously observed or studied with regard to the sputtering yields of neutrals, which are orders of magnitude higher than those of ionized species. It is worth noting that Martinez et al. (2019) considered a positively charged 90 keV ion beam as a projectile and quantified the ionic component of desorption. In contrast, the current work considers a 2–5 keV electron beam and the neutral component of the desorption. Therefore, differences between the two works are expected.

Another investigation comparing the irradiation of amorphous and crystalline ices (CH_3OH and N_2O ices) was conducted by Mifsud et al. (2022a). The authors observed that the strong and extensive hydrogen-bonding network present in crystalline ices appears to significantly protect this phase from radiation-induced decay. According to the authors, some of the energy from the incident electrons must be used to disrupt the hydrogen-bonding network before initiating radiolytic chemistry. The authors concluded their work by suggesting that crystalline water ice is less sensitive to the processing by radiation than amorphous ice.

Zheng et al. (2007) in a study of electron bombardment of crystalline and amorphous deuterated water ices at 12 K suggested that the structure of the water ice influences the production rates of molecular oxygen, molecular hydrogen, and hydrogen peroxide under irradiation. Additionally, they observed that the production rates of D_2, O_2, and D_2O_2 in amorphous ices are systematically higher than those in crystalline samples. However, in both ices, they found that the production rates of H_2, O_2, and H_2O_2 (and their respective deuterated species) decrease as the temperature rises, which was also observed in their previous work on the irradiation of crystalline H_2O ice (Zheng et al. 2006). Such differences, when considering individual values of rate constants, can also be observed when we compare the current results for crystalline water ice with the ones calculated by (Da Silveira & Pilling, in preparation) for amorphous water ice irradiated by electrons.

3.4 The CE phase at different temperatures

When an astrophysical ice is subjected to a constant temperature and exposed to a large fluence of radiation, it can eventually reach a phase called CE as largely discussed elsewhere (e.g. Almeida et al. 2017; Bonfim et al. 2017; Rachid et al. 2017; Vasconcelos et al. 2017a, b, c; Pilling et al. 2019; Carvalho & Pilling 2020a, b; Freitas & Pilling 2020; Rachid et al. 2020). During this stage, the abundances of the molecules within the ice remain constant, even when further irradiation occurs. This phenomenon is the result of a balance between the production of new molecules from radiolysis and the destruction of molecules from subsequent reactions. It is worth noting that ices under this phase presents some liquids' behavior, including non-zero viscosity and large molecular diffusion, homogeneity, constant radiation-induced desorption (reminds vapor pressure) and can be called as liquid astrophysical ice (see also Ghesquière et al. 2015; Tachibana et al. 2017; Rosu-Finsen et al. 2023)

The precise composition of the equilibrium state depends on various factors, such as the initial molecular abundances, the type of incoming radiation, radiation fluence and energy, and the presence of other species in the ice. The study of CE in astrophysical ices can provide insights into the evolution of these ices in various interstellar environments, such as protostellar regions and molecular clouds. In particular, it can help to understand the formation of complex organic molecules that are detected in these environments and provide clues to the processes that give rise to the rich diversity of organic chemistry observed in the Universe.

In the following sections, we will discuss the CE phase, including the molecular abundances and desorption to gas-phase, of the studied crystalline water ice irradiated by 5 keV electrons at different temperatures.

3.4.1 Molecular abundances

Fig. 8 illustrates the percentages of molecular abundances in the crystalline water ice under study at the CE phase, after being bombarded by 5 keV electrons at varying temperatures. H_2O molecule constitutes

Table 3. Comparisons between the average values obtained by PROCODA from electron bombardment of amorphous and crystalline H_2O ices at very low temperatures.

Average parameter	Crystalline H_2O ice at 12 K irradiated by 5 keV electrons (this work)	Amorphous H_2O ice at 20 K irradiated by 2 keV electrons (Da Silveira & Pilling, in preparation)
ERC for the intrinsic desorption reactions (k_{des})	1.4e-6 s^{-1}	1.2e-6 s^{-1}
ERC for radiation-induced dissociation reactions	5.8e-2 s^{-1}	9.6e-2 s^{-1}
ERC for the bimolecular reactions	2.5e-24 cm^3 $molecules^{-1}$ s^{-1}	9.1e-24 cm^3 $molecules^{-1}$ s^{-1}
Desorption rate	5.6e + 11 molecules s^{-1}	9.5e + 10 molecules s^{-1}
Desorption yield (Y)	~1e-2 molecules $electrons^{-1}$	3.2e-4 molecules $electrons^{-1}$

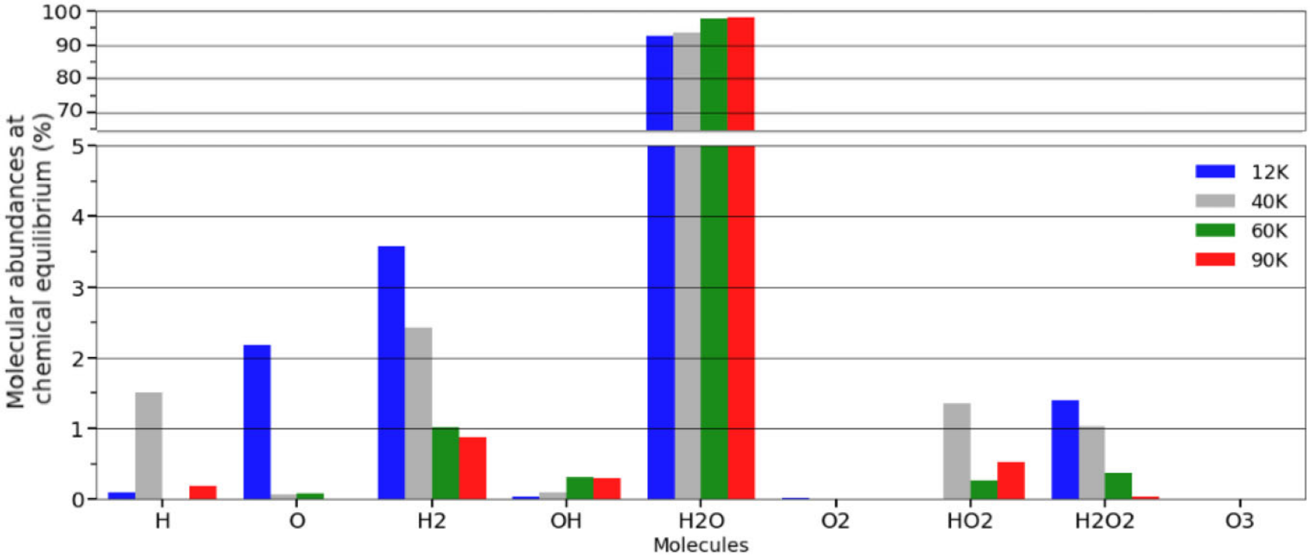

Figure 8. Molecular abundances at the CE phase (= equilibrium branching ratio EBR) expressed as a percentage, obtained by the best-fitting models. Colours indicate the four type of crystalline water ice studied with temperatures ranging from 12 to 90 K (experimental data taken from Zheng et al. 2006).

the principal component, accounting for more than 90 per cent of the total abundance within the irradiated ice. Interestingly, the abundance of H_2O and the hydroxyl radical OH (a minor component) increases with the increase in ice's temperature, while the opposite trend is observed for the produced H_2O_2 and H_2.

The abundance of H_2O, which is the dominant species in the ice, increases with increasing temperature, which is consistent with the idea that thermal processes favor its production. Similarly, the abundance of the minor component OH also increases with temperature, which is likely due to the fact that OH can be produced from H_2O through radiolysis. On the other hand, the abundance of H_2O_2 and H_2, which are also produced during radiolysis, decreases with increasing temperature. This is likely because these species can react with other radicals in the ice, which become more abundant at higher temperatures, leading to their removal.

Comparing the molecular abundance of the four studied ices we observe that the O atoms produced by radiation are largely abundant in the cold ice and less abundant in the hotter ices. This behavior might be due to the fact that the O atoms produced by radiation are more likely to remain in the cold ice than in the hotter ices (this could also be the case for the abundant H atoms at 40 K). In cold ice, the molecules are more tightly bound together, making it more difficult for the O atoms to escape. In hotter ices, the molecules are more loosely bound together, allowing the O atoms to escape more easily. Additionally, the O atoms produced by radiation are more likely to react with other molecules in the hotter ices, further reducing their abundance. An alternative explanation for this enhancement of O atoms at cold temperatures might be related to the fact that the energy of the fast electrons could be more efficiently absorbed by the cold ice, leading to a more efficient dissociation of the water molecules into O atoms. Further investigation may help to elucidate this issue.

The models also show that the abundances of O_2 and O_3 are virtually negligible at the CE phase. A possible explanation for this behavior might be related to a large endothermicity of the net electron-induced reactions that form these molecules in the radiolysis of ice dominated by water, and also to the presence of larger energy barriers in such reactions to be overcome.

3.4.2. The dominant reactions for molecular consumption and production

Following Zheng et al. (2006) the electron destruction of water molecules in experiments is the dominant source of OH radicals, as H_2O_2 has a much lower concentration than H_2O. The destruction of H_2O_2 can also contribute to the reduction of products, but the main factor that lowers the production rates at higher temperatures is the recombination of OH and H. This recombination is thermally activated and competes with the formation of products such as O_2 and H_2O_2.

The production and consumption of studied species at CE are important factors in understanding the dynamics of a chemical system. It is essential to understand the dominant reactions that occur in order to accurately predict the behavior of the system. In this section, we will discuss the dominant reactions for production and consumption of the studied species at CE and how they can be used to better understand the system.

Table 4 lists the dominant reactions for the consumption and production of the studied species at the CE obtained by the best-fitting models on the data of crystalline H_2O ice irradiated by 5 keV electrons. The percentage values were calculated directly from the respective contributions of such reactions in the chemically coupled system of equations (see equation 1) for each suited species. The contribution of the desorption reaction, in percentage, is also presented in this table.

The production and consumption of reactive species in astrophysical ices play a crucial role in the chemical evolution of interstellar environments. Our results demonstrate that the HO_2 species is crucial for the production of O_2, while the H_2O_2 species is important for the production of HO_2. Furthermore, we observed that the primary consumption of O is due to its collision reactions with H_2O. On the other hand, the primary production of H_2O_2 is due to collision reactions of H_2O with O atoms.

We also investigated the contribution of desorption to the consumption of H_2O, HO_2, OH, and H_2O_2. Our findings indicate that the contribution of desorption to the consumption of H_2O, HO_2, and OH exhibits a clear correlation with increasing temperature. However, there is no clear correlation between the contribution of desorption and temperature for H_2O_2.

Our results shed light on the complex interplay of reactive species and their importance for the production and consumption of key molecular species in astrophysical ices. This study provides important insights into the chemical processes that occur in interstellar environments and highlights the crucial role of reactive species in the evolution of these environments.

3.4.3. *The induced-radiation molecular desorption to gas-phase*

Fig. 9 illustrates the molecular desorption at CE obtained by the best-fitting models for four different types of crystalline water ice with temperatures ranging from 12 to 90 K [the experimental data were taken from Zheng et al. (2006)]. The colour coding allows for easy differentiation between the different types of ice. Panel (a) displays the molecular desorption in percentage for each of the four types of crystalline water ice studied. When bombarded by 5 keV electrons, the water molecules exhibit the highest desorption yield among the studied species, constituting the dominant desorbed species. In contrast, the contribution of other radiation products to the total desorption yield is negligible, representing less than 1 per cent of the total desorption. However, in astronomical scenarios, even such low contributions can be significant and observable.

Panel (b) shows that when crystalline water ice is bombarded with energetic electrons, the amount of molecules desorbed per electron varies depending on the species. H_2O has the highest desorption yield, which means that it is the most easily desorbed species, with about 1 molecule desorbed per 100 electrons. This indicates that H_2O is more likely to be present in the gas phase in astrophysical environments, where crystalline water ice is subject to energetic electron bombardment. On the other hand, the desorption yield of all other studied species is much lower, with less than 1 molecule desorbed per 10 000 electrons.

The desorption yield of a species upon energetic electron bombardment is influenced by various factors, including temperature, the specific characteristics of the ice structure, such as density, and the available neighbours' species within the ice. In the case of O_2 and O_3, their molecular desorption yields at CE are very low (around 2e-9 molecules per electron) and do not appear to be affected by temperature.

Fig. 9(b) also shows that the desorption yield of H_2O_2 and H_2 decreases as the ice´s temperature increases. This is likely due to an increase in the molecular mobility of these species at higher temperatures, which leads to their re-adsorption onto the ice surface or reactions with other species. Additionally, the higher temperature may also result in the formation of larger ice grains, which can lead to a reduction in the surface area available for the desorption of these species. Therefore, the desorption yield of H_2O_2 and H_2 is temperature-dependent and should be considered when investigating the chemical processes that occur in astrophysical environments. As the temperature of the ice rises, the desorption of OH and HO_2 also becomes more pronounced.

Andersson et al. (2005) have presented a theoretical model of the dynamics of crystalline water ice at 10 K in the presence of UV photons. The authors observed that photoproducts such as H atoms and OH radicals can diffuse through the water ice tens of angstroms before being trapped or desorbed. The authors also discuss that specific reaction routes may arise depending on the energy available in the collision between moving species and H_2O targets within the ice.

As discussed in the previous section, we observed that the primary production of H_2O_2 is due to collision reactions of H_2O with O atoms within the irradiated ices. Therefore, understanding the temperature-dependent desorption of H_2O and O atoms is also crucial for modeling the formation and distribution of H_2O_2 and other water radiolysis products in astrophysical environments.

Overall, this study provides insight into the desorption of molecules in astrophysical environments and the factors that influence it. These findings can be used to refine astrophysical models and aid in the interpretation of astronomical observations of water ice in space.

4 ASTROPHYSICAL IMPLICATIONS

Research on reaction rates and molecular abundances in astrophysical ices is crucial to understanding the chemical evolution of interstellar and planetary environments. In this sense, the determination of such parameters in both amorphous and crystalline water ices is of great importance, since they are widespread in interstellar environments and play a significant role in the formation of comets and planetary bodies. The current work sheds light on the temperature dependence of reaction rates and molecular abundances in crystalline water ice under irradiation by 5 keV electrons. Since astrophysical ices may have different temperatures, such investigations will allow a better understanding of the complexity of the ISM.

In this manuscript, we study the effects of 5 keV electrons on crystalline water ices (data from Zheng et al. 2006) at different temperatures, simulating their bombardment by energetic electrons from various sources, including stellar particles and cosmic rays. It is worth noting that this study may also be applied to consider the effects of protons and other ionic components of cosmic rays, which induce chemical changes within the irradiated ices and also the ice's exposure to X-rays. Following Pilling et al. (2010a, b) and

Table 4. Dominant reactions considered in the mapping of the chemical evolution of crystalline H_2O ice irradiated by 5 keV electrons at different temperatures (data from Zheng et al. 2006) at the CE phase reached at high radiation fluence for the consumption and production of the studied species.

Species	Ice temp.	Main consumption reactions** (reaction label; per cent)	Main production reactions (reaction label; per cent)
H	12 K	$H + H_2O \rightarrow H_2 + OH$ (r21; $\sim$81 per cent) R42 (12 per cent) Desorption (1.9e-6 per cent)	$OH + RAD \rightarrow H + O$ (r41; 53 per cent)* R9 (38 per cent)
	40 K	$H + H \rightarrow H_2$ (r18; 89 per cent)* (r10; 7.1 per cent) Desorption (5.3e-5 per cent)	$H_2 + RAD \rightarrow H + H$ (r17; 96 per cent) (r41; 2.1 per cent)
	60 K	$H + H_2O \rightarrow H_2 + OH$ (r21; $\sim$100 per cent) (r10; 0.1 per cent) Desorption (1.5e-7 per cent)	$H_2 + OH \rightarrow H + H_2O$ (r22; 39 per cent)* (r9; 30 per cent)
	90 K	$H + H \rightarrow H_2$ (r18; 45 per cent)* $H + H_2O \rightarrow H_2 + OH$ (r21; 37 per cent) Desorption (3.9e-4 per cent)	$H_2 + OH \rightarrow H + H_2O$ (r22; 77 per cent)* (r43; 16 per cent)
O	12 K	$O + H_2O \rightarrow H_2O_2$ (r7; $\sim$92 per cent) R14 (4 per cent) Desorption (2.6e-6 per cent)	$H_2O_2 + RAD \rightarrow O + H_2O$ (r8; 93 per cent)* R13 (3.6 per cent)
	40 K	$O + H_2O \rightarrow H_2O_2$ (r7; $\sim$97 per cent) (r14; 2.5 per cent) Desorption (1.3e-8 per cent)	$H_2O_2 + RAD \rightarrow O + H_2O$ (r8; 92 per cent)* (r13; 3.8 per cent)
	60 K	$O + H_2O \rightarrow H_2O_2$ (r7; $\sim$97 per cent) (r14; 2.6 per cent) Desorption (9.3e-7 per cent)	$H_2O_2 + RAD \rightarrow O + H_2O$ (r8; 98 per cent)* (r13 $\sim$2 per cent)
	90 K	$O + H_2O \rightarrow H_2O_2$ (r7; $\sim$95 per cent) (r14; 3.4 per cent) Desorption (5.8e-8 per cent)	$H_2O + RAD \rightarrow H_2 + O$ (r13; 84 per cent) (r8; 13 per cent)
H_2	12 K	$H_2 + O \rightarrow H_2O$ (r14; 97 per cent) (r40; 1.5 per cent) Desorption (1.4e-3 per cent)	$H_2O + RAD \rightarrow H_2 + O$ (r13; 85 per cent) R21(15 per cent)
	40 K	$H_2 + RAD \rightarrow H + H$ (r17; 92 per cent) (R14; 6.7 per cent) Desorption (2.7e-4 per cent)	$H + H \rightarrow H_2$ (r18; 86 per cent) (r13; 11 per cent)
	60 K	$H_2 + O \rightarrow H_2O$ (r14; 82 per cent)* (r22; 14 per cent) Desorption (1.0e-2 per cent)	$H_2O + RAD \rightarrow H_2 + O$ (r13; 67 per cent) (r21, 33 per cent)
	90 K	$H_2 + OH \rightarrow H + H_2O$ (r22; 94 per cent)* (r17; 3.8 per cent) Desorption (5.2e-3 per cent)	$H_2O + RAD \rightarrow H_2 + O$ (r13; 44 per cent) (r21; 35 per cent)
OH	12 K	$OH + RAD \rightarrow H + O$ (r51; per cent) R9 (37 per cent) Desorption (5.9e-7 per cent)	$H + H_2O \rightarrow H_2 + OH$ (r21; 78 per cent)* R42(12 per cent)
	40 K	$OH + RAD \rightarrow H + O$ (r41; 29 per cent)* (r35; 27 per cent) Desorption (4.9e-7 per cent)	$H + H_2O_2 \rightarrow OH + H_2O$ (r10; 91 per cent)* (r38; 6.9 per cent)
	60 K	$OH + H_2O_2 \rightarrow H_2O + HO_2$ (r35; 32 per cent)* $H_2 + OH \rightarrow H + H_2O$ (r22; 32 per cent) Desorption (1.9e-3 per cent)	$H + H_2O \rightarrow H_2 + OH$ (r21; 72 per cent)* (r12; 13 per cent)
	90 K	$H_2 + OH \rightarrow H + H_2O$ (r22; 80 per cent)* (r6; 16 per cent) Desorption (8.6e-4 per cent)	$H_2O_2 + RAD \rightarrow OH + OH$ (r12; 56 per cent)* $H + H_2O \rightarrow H_2 + OH$ (r21; 38 per cent)
H_2O	12 K	$O + H_2O \rightarrow H_2O_2$ (r7; 94 per cent)* $H_2O + RAD \rightarrow H_2 + O$ (r13; 3.8 per cent) Desorption (2.3e-2 per cent)	$H_2O_2 + RAD \rightarrow O + H_2O$ (r8; 95 per cent) $H_2 + O \rightarrow H_2O$ (r14; 4.1 per cent)
	40 K	$O + H_2O \rightarrow H_2O_2$ (r7; 95 per cent)* (r13; 3.6 per cent) Desorption (0.2 per cent)	$H_2O_2 + RAD \rightarrow O + H_2O$ (r8; 90 per cent) (r10; 4.8 per cent)
	60 K	$O + H_2O \rightarrow H_2O_2$ (r7; 95 per cent)* (r13; 2.5 per cent) Desorption (0.7 per cent)	$H_2O_2 + RAD \rightarrow O + H_2O$ (r8; 97 per cent) (r14 2.4 per cent)
	90 K	$O + H_2O \rightarrow H_2O_2$ (r7; 30 per cent)* $H_2O + RAD \rightarrow H_2 + O$ (r13; 28 per cent) Desorption (17 per cent)	$H_2 + OH \rightarrow H + H_2O$ (r22; 72 per cent)* (r6; 15 per cent)

Table 4 – *continued*

Species	Ice temp.	Main consumption reactions** (reaction label; per cent)	Main production reactions (reaction label; per cent)
O_2	12 K	$H_2O + O_2 \rightarrow O + H_2O_2$ (r28; 54 per cent) R1 (41 per cent) Desorption (2.7e-8 per cent)	(R2; 70 per cent) (r27, 29 per cent)
	40 K	$H_2O + O_2 \rightarrow O + H_2O_2$ (r28; 37 per cent) (r1; 33 per cent) Desorption (1.4e-8 per cent)	$H + HO_2 \rightarrow H_2 + O_2$ (r45; 42 per cent)* (r33; 42 per cent)
	60 K	$H_2O + O_2 \rightarrow O + H_2O_2$ (r28; 64 per cent) (r38; 23 per cent) Desorption (1.2e-11 per cent)	$HO_2 + RAD \rightarrow H + O_2$ (r33; 53 per cent)* (r39; 40 per cent)
	90 K	$H_2O + O_2 \rightarrow OH + HO_2$ (r38; 40 per cent) (r1; 39 per cent) Desorption (8.6e-12 per cent)	$HO_2 + RAD \rightarrow H + O_2$ (r33; 74 per cent)* (r39; 22 per cent)
HO_2	12 K	(R31; 57 per cent) $H_2O + HO_2 \rightarrow OH + H_2O_2$ (r36; 31 per cent) Desorption (1.2e-8 per cent)	$OH + H_2O_2 \rightarrow H_2O + HO_2$ (r35; 77 per cent)* (R38, 19 per cent)
	40 K	$H + HO_2 \rightarrow H_2 + O_2$ (r45; 42 per cent)* (r33; 41 per cent) Desorption (6.3e-4 per cent)	$OH + H_2O_2 \rightarrow H_2O + HO_2$ (r35; ~80 per cent)* (r38; 20 per cent)
	60 K	$H_2O + HO_2 \rightarrow OH + H_2O_2$ (r36; 62 per cent) (r31; 36 per cent) Desorption (9.2e-3 per cent)	$OH + H_2O_2 \rightarrow H_2O + HO_2$ (r35; 82 per cent)* (r43; 16 per cent)
	90 K	$H_2O + HO_2 \rightarrow OH + H_2O_2$ (r36; 49 per cent) (r31; 49 per cent) Desorption (3.8e-2 per cent)	$H_2O_2 + RAD \rightarrow H + HO_2$ (r43; 83 per cent) (r35; 15 per cent)
H_2O_2	12 K	$H_2O_2 + RAD \rightarrow O + H_2O$ (r8; 99 per cent) (r27, 0.6 per cent) Desorption (1.2e-5 per cent)	$O + H_2O \rightarrow H_2O_2$ (r7; 98 per cent) (r28; 1.2 per cent)
	40 K	$H_2O_2 + RAD \rightarrow O + H_2O$ (r8; 93 per cent) (r10; 5 per cent) Desorption (5.5e-6 per cent)	$O + H_2O \rightarrow H_2O_2$ (r7; 98 per cent) (r28; 0.6 per cent)
	60 K	$H_2O_2 + RAD \rightarrow O + H_2O$ (r8; 99 per cent) (r35; 0.4 per cent) Desorption (2.0e-5 per cent)	$O + H_2O \rightarrow H_2O_2$ (r7; 99 per cent) (r9; 0.4 per cent)
	90 K	$H_2O_2 + RAD \rightarrow OH + OH$ (r12; 49 per cent) (r43; 29 per cent) Desorption (4.2e-6 per cent)	$O + H_2O \rightarrow H_2O_2$ (r7; 96 per cent) (r36, 2.9 per cent)
O_3	12 K	$O_3 + RAD \rightarrow O + O_2$ (r3; 96 per cent) (r26; 2.3 per cent) Desorption (2.4e-11 per cent)	(r4; 98 per cent) $OH + O_2 \rightarrow H + O_3$ (r48; 1.5 per cent)
	40 K	$O_3 + RAD \rightarrow O + O_2$ (r3; 97 per cent) (r26; 1.2 per cent) Desorption (7.2e-11 per cent)	$OH + O_2 \rightarrow H + O_3$ (r48; 74 per cent)* (r4; 26 per cent)
	60 K	$O_3 + RAD \rightarrow O + O_2$ (r3; 99 per cent) (r24; 0.4 per cent) Desorption (2.1e-12 per cent)	$O + H_2O_2 \rightarrow H_2 + O_3$ (r25; 64 per cent)* (r50; 29 per cent)
	90 K	$O_3 + RAD \rightarrow O + O_2$ (r3; ~100 per cent) (r24; ~0.1 per cent) Desorption (1.2e-13 per cent)	$O + HO_2 \rightarrow H + O_3$ (r50; 94 per cent)* (r23; 3.5 per cent)

*Dominant reaction has changed during ice irradiation.

**Desorption in percentage is also listed. The contribution of the desorption reaction, in percentage, is also presented.

Pilling & Bergantini (2015), cosmic rays and X-rays drive chemical changes within astrophysical ices mainly due to collisions between the produced secondary electrons and the frozen molecules.

The ices studied at 12 K have direct application in astrophysical ices that experience thermal heating followed by cooling processes, for example by being obscured by gas/dust and less exposed to radiation. This is observed in protostellar discs where ices are largely exposed to radiation at the outer border of the disc but, due to disc turbulence, might move to inner obscured regions (cold regions deep into the disc). Another scenario for crystalline water ice at low temperatures is comets when they are far from the central star.

The warm crystalline ice (90 K) is relevant for simulating the chemical processing of water ices on the moons Europa, Ganymede, and Callisto. Zheng et al. (2006) estimated that the incident energy deposited by 5 keV electrons (with a current of 10 000 nA) on the studied ices at maximum fluence (after 180 min of irradiation) was about 1.7e21 eV cm^{-2}. This corresponds to an energy deposition of about 10 months on Europa's surface, 250 yr on Callisto, 10 yr on

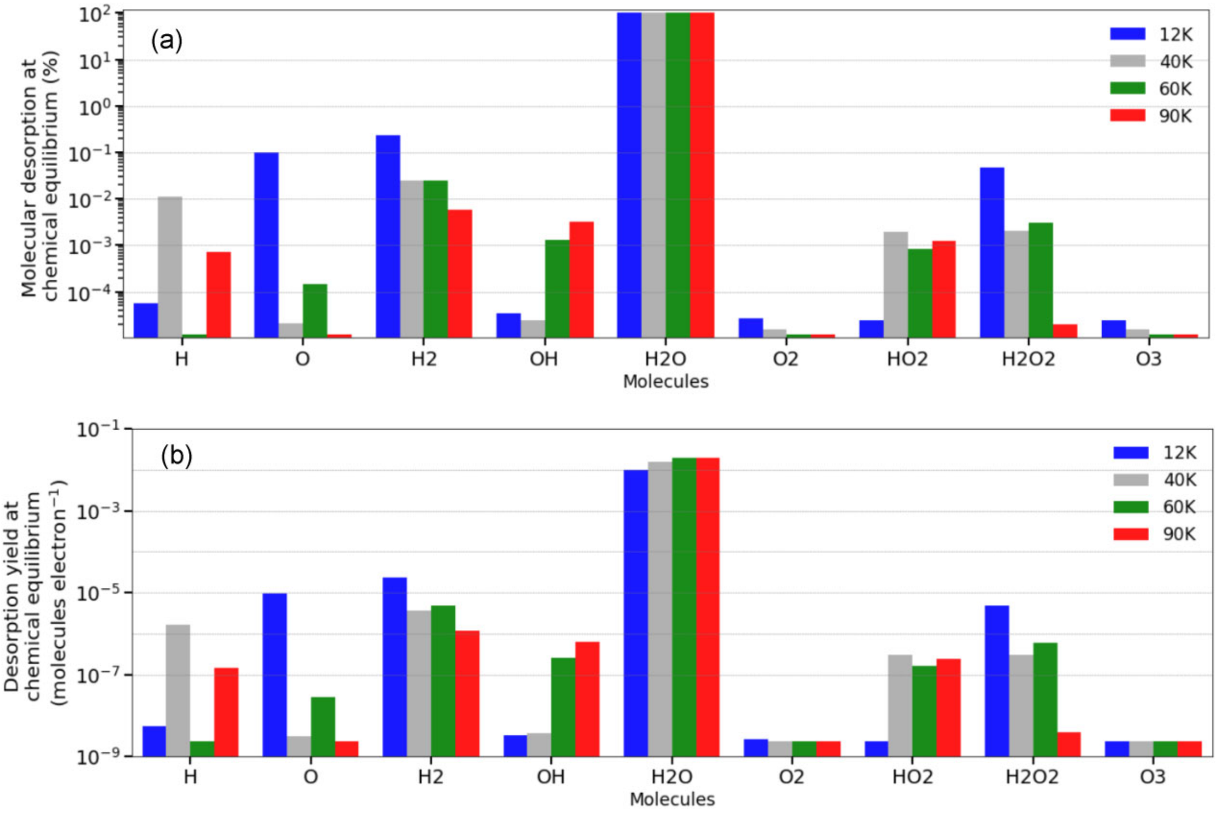

Figure 9. Molecular desorption at CE, obtained by the best-fitting models. Colours indicate the four crystalline water ices studied with temperatures ranging from 12 to 90 K (experimental data taken from Zheng et al. 2006). Panel (a) indicates the molecular desorption in percentage. Panel (b) indicates molecular desorption yield in units (molecules per electron) considering the total desorption yield in each model (see also Fig. 7).

Ganymede's polar cap, and 200 yr on Ganymede's equator, according to energy fluxes provided by Cooper et al. (2001).

Hori and Hondoh (2003) predicted that the diffusion coefficient of hydrogen, oxygen, and other molecular species depends on the crystal structure of water, i.e. crystalline versus amorphous. Hence, it is crucial to examine how the crystal structure affects the formation rates of hydrogen, oxygen, and hydrogen peroxide at different temperatures.

The calculated reaction rates and desorption rates have significant astrophysical implications, as they can be employed in astrochemical models (e.g. Du et al. 2012; Rocha et al. 2023) to simulate the chemical evolution of interstellar and planetary environments. For example, the determination of the reaction rate of a specific chemical pathway can help to predict the abundance of a particular molecule in interstellar environments. The desorption rates are also crucial to understanding the delivery of molecules from interstellar ices to the gas phase, which plays a fundamental role in the formation of comets and planetary bodies.

Besides the calculated ERCs, the desorption yield derived in this work might help to understand the presence of H_2O_2 and other products from bombardment of crystalline water ices on the frozen moons of Galilean planets (see also Noll et al. 1996; Barth et al. 1997; Calvin and Spencer 1997; Carlson et al. 1999; Hendrix et al. 1999). The current study may also be employed to constrain the abundance of H_2O_2, in the ISM detected at gas-phase by the *APEX* telescope toward the core of protostar ρ Oph A (e.g. Bergman et al. 2011).

Historically, the formation of H_2O_2 was claimed to be due to successive hydrogen additions to O_2 ices. This was first proposed by Tielens & Hagen (1982), based on theoretical arguments, and later experimentally investigated by other authors, such as Miyauchi et al. (2008) and Ioppolo et al. (2008). However, several other laboratory experiments have pointed out that this species might also be formed by the processing of water-rich ices by ionizing radiation (e.g. Loeffler et al. 2006; Pilling et al. 2010; Pillign & Bergantini 2015; Kulikov et al. 2019; Pilling & da Silva, 2023; and references therein). Therefore, understanding the dominant reaction routes to produce and consume this species (and others) in water-rich ices under processing by radiation helps to clarify the abundance of this species in the ISM.

5 CONCLUSION

In this manuscript, we present a theoretical model that uses the PROCODA code to map the chemical evolution and kinetics of crystalline H_2O ice irradiated with 5 keV electrons at different temperatures ranging from 12 to 90 K. The experimental data used in our study were taken from Zheng et al. (2006). The main conclusions of our study are as follows:

1) The irradiation of crystalline water ice by 5 keV electrons leads to the formation of various molecular species, including those non-observed in the experiments but predicted (H, O, OH, HO_2). Additionally, different reaction routes exhibit distinct temperature dependencies, which can be attributed to the specific reaction mechanisms involved, ice density, and the presence of specific neighbours.

2) The average ERCs for radiation induced dissociation decreases as the ice´s temperature increase ranging from 0.06 s^{-1} for the coldest studied ice to 0.01 s^{-1} to the warmest ice. This behavior was also

noticed with less strength also for the ERCs of bimolecular collisions, ranging from 4 to 1.5e-24 cm^3 $molecules^{-1}$ s^{-1} for the studied ices. Curiously, the average ERCs of radiation-induced reactions increased with increasing ice temperature.

3) The abundance of molecular species in the ice at CE and its desorption to gas-phase depend on both the temperature of the ice.

4) At CE phase, the dominant reaction was highlighted. For example, the abundance of HO_2 is crucial for the production of O_2, and the H_2O_2 molecule is important for the production of HO_2. The main production of H_2O_2 is due to collision reactions of H_2O with O.

5) H_2O molecules are the dominant desorbed species with a desorption yield of about 1 molecule per 100 electrons and seem to be enhanced as for warmer crystalline ices. On the other hand, the desorption yield of H_2O_2 and H_2 decreases as the ice temperature increases.

6) The comparison with a similar study employing the PROCODA on amorphous H_2O ice, also irradiated by electrons, indicates that crystalline ice has a lower value of ERCs for both radiation-induced dissociation and bimolecular reactions compared to amorphous ice. The largest difference was observed in molecular desorption, where the desorption rate in crystalline ice was approximately five times larger than the calculated value for the amorphous sample. Furthermore, the desorption yield in crystalline ice was significantly higher than the value of obtained for the amorphous sample.

These conclusions have important implications for astrochemistry, as they provide insight into the chemical processes occurring in interstellar environments, such as protoplanetary discs and comets. For example, the calculated reaction rate constants and desorption rates can be incorporated into astrochemical models to better understand the formation and evolution of molecular species in these environments. Finally, the research presented in this work provides valuable insights into the temperature dependence of reaction rates and molecular abundances in crystalline ices under electron irradiation. The obtained results have significant astrophysical implications and can be employed in models to simulate the chemical evolution of interstellar and planetary environments, helping us to understand the complex processes that shape the universe around us.

ACKNOWLEDGEMENTS

The authors acknowledge the Brazilian research agencies Conselho Nacional de Desenvolvimento Científico e Tecnológico–CNPq (#302985/2018–2; #302608/2022–2; #302939/2022–9) and Coordenação de Aperfeiçoamento de Pessoal de Nível Superior–CAPES (#PDPG/88887.691437/2022–00).

DATA AVAILABILITY

The data underlying this article will be shared on reasonable request to the corresponding author.

REFERENCES

Almeida G. C., Pilling S., De Barros A. L. F., Da Costa C. A. P., Pereira R. C., Da Silveira E. F., 2017, MNRAS, 471, 1330

Andersson S., Kroes G.-J., Van Dishoeck E. F., 2005, Chem. Phys. Lett., 408, 415

Andrade D. P. P. et al. 2008, J. Phys. Chem. C, 112, 11954

Barth C. A. et al. 1997, Geophys. Res. Lett., 24, 2147

Barucci M. A., Dalle Ore C. M. , Perna D., Cruikshank D. P., Doressoundiram A., Alvarez-Candal A., Dotto E., Nitschelm C., 2015, A&A, 584, A107

Bennett C. J., Jamieson C. S., Kaiser R. I., 2009. Phys. Chem. Chem. Phys., 11, 4210

Bennett C. J., Jamieson C. S., Kaiser R. I., 2010, Phys. Chem. Chem. Phys., 12, 4032

Berdis J. R., Gudipati M. S., Murphy J. R., Chanover N. J., 2020, Icarus, 341, 113660

Bergman P., Parise B., Liseau R., Larsson B., Olofsson H., Menten K. M., Güsten R., 2011, A&A, 531, L8

Boogert A. C. A. et al. 2008, ApJ, 678, 985

Bossa J. B., Paardekooper D. M., Isokoski K., Linnartz H., 2015. Phys. Chem. Chem. Phys., 17, 17346

Brown R. H. et al., 2006, Science, 311, 1425

Calvin W. M., Spencer J. R., 1997, Icarus, 130, 505

Carlson R. W. et al., 1999, Science, 283, 2062

Carvalho G. A., Pilling S., 2020a, J. Phys. Chem. A, 124, 8574

Carvalho G. A., Pilling S., 2020b, MNRAS, 498, 689

Carvalho G. A., Pilling S., Galvão B. R. L., 2022, MNRAS, 515, 3760

Cook J. C., Desch S. J., Roush T. L., Trujillo C. A., Geballe T. R., 2007, ApJ, 633, 1406

Cooper J., 2001, Icarus, 149, 133

Dartois E., 2005, Space Sci. Rev., 119, 293

Dartois E. et al., 2015, A&A, 576, A125

De Marcellus P. et al. 2011, ApJ, 727, L27

De Souza Bonfim V., Barbosa De Castilho R., Baptista L., Pilling S., 2017, Phys. Chem. Chem. Phys., 19, 26906

Du F., Parise B., Bergman P., 2012, A&A, 538, A91.

Emery J. P., Burr D. M., Cruikshank D. P., Brown R. H., Dalton J. B., 2005, A&A., 435, 353

Famá M., Loeffler M. J., Raut U., Baragiola R. A., 2010, Icarus, 207, 314

Freitas M. F., Pilling S., 2020, Quimica Nova, 43, 521

Garcia A., Meinert C., Sugahara H., Jones N., Hoffmann S., Meierhenrich U., 2019, Life, 9, 29

Ghesquière P., Mineva T., Talbi D., Theulé P., Noble J. A., Chiavassa T., 2015, Phys. Chem. Chem. Phys., 17, 11455

Gibb E. L., Whittet D. C. B., Boogert A. C. A., Tielens A., 2004, ApJS, 151, 35

Hansen G. B., McCord T. B., 2004, J. Geophys. Res.: Planets, 109, E01012

Hendrix A. R., Barth C. A., Stewart A. I. F., Hord C. W., Lane A. L., 1999, Lunar Planet. Sci. Conf., 30, 2043

Herbst E., Garrod R. T., 2022, Frontiers Astron. Space Sci., 8, 209

Hori A., Hondoh T., 2003, Canadian J. Phys., 81, 251

Ilee J. D. et al., 2021, ApJSS, 257, 9

Ioppolo S., Cuppen H. M., Romanzin C., Van Dishoeck E. F., Linnartz H., 2008, ApJ, 686, 1474

Jamieson C. S., Mebel A. M., Kaiser R. I., 2006, ApJSS, 163, 184

Jenniskens P., Blake D. F., 1996, ApJ, 473, 1104

Jenniskens P., Blake D. F., Kouchi A., 1998, Solar System Ices: Based on Reviews Presented at the International Symposium. Springer, The Netherlands, p. 139

Jewitt D. C., Luu J., 2004, Nature, 432, 731

Johnson R. E., Quickenden T. I., 1997, J. Geophys. Res.: Planets, 102, 10985

Justtanont K., Olofsson G., Dijkstra C., Meyer A. W., 2006, A&A, 450, 1051

Kouchi A., Kuroda T., 1990, Nature, 344, 134

Kouchi A., Yamamoto T., Kozasa T., Kuroda T., Greenberg J. M., 1994, A&A, 290, 1009

K Schmidt K. G., Dahl-Jensen D., 2003, Ann. Glaciol., 37, 129

Kulikov M. Y., Feigin A. M., Schrems O., 2019, Sci. Rep., 9, 11375

Ladd-Parada M. et al. 2022, J. Phys. Chem. B, 126, 2299

Leto G., Baratta G. A., 2003, A&A, 397, 7

Loeffler M., Raut U., Vidal R., Baragiola R., Carlson R., 2006,. Icarus, 180, 265

Lombaert R. et al., 2013, A&A, 554, A142

Lunine J. I., 2006, in Lauretta D. S., McSween H. Y., Jr., eds, Meteorites and the Early Solar System II. Univ. Arizona Press, Tucson, AZ, p. 309

Mcclure M. K. et al., 2023, Nature Astron., 431, 7

Malfait K., Waelkens C., Bouwman J., de Kouter A., Waters L., 1999. A&A, 345, 181

Martinez R. et al. 2019. J. Phys. Chem. A, 123, 8001

Mastrapa R., Brown R., 2006, Icarus, 183, 207

Meier R. M., Loeffler M. J., 2020, Surf. Sci., 691, 121509

Mejía C., De Barros A. L. F., Rothard H., Boduch P., Da Silveira E. F., 2022, MNRAS, 514, 3789

Mifsud D. V. et al. 2022a, Phys. Chem. Chem. Phys., 24, 10974

Mifsud D. V. et al. 2022b, Eur. Phys. J. D, 76, 87

Miyauchi N., Hidaka H., Chigai T., Nagaoka A., Watanabe N., Kouchi A., 2008, Chem. Phys. Lett., 456, 27

Moore M. H., Hudson R. L., 1992, ApJ, 401, 353

Mousis O. et al., 2016, ApJ, 819, L33

Noll K. S., Johnson R. E., Lane A. L., Domingue D. L., Weaver H. A., 1996, Science, 273, 341

Nuevo M., Auger G., Blanot D., D'hendecourt L., 2008, Orig. Life Evol. Biosph., 38, 37

Öberg K. I., Boogert A. C. A., Pontoppidan K. M., Van Den Broek S., Van Dishoeck E. F., Bottinelli S., Blake G. A., Evans N. J., 2011, ApJ, 740, 109

Paranicas C., Carlson R. W., Johnson R. E., 2001, Geophys. Res. Lett., 28, 673

Pilling S., Bergantini A., 2015, ApJ, 811, 151

Pilling S., Freitas F. M., 2023, Revista Univap, 29, 61

Pilling S., Andrade D. P. P., Neto Á. C., Rittner R., Naves De Brito A., 2009, J. Phys. Chem. A, 113, 11161

Pilling S., Duarte E. S., Domaracka A., Rothard H., Boduch P., Da Silveira E. F., 2011, Phys. Chem. Chem. Phys., 13, 15755

Pilling S., Seperuelo Duarte E. , Domaracka A., Rothard H., Boduch P., da Silveira E. F., 2010a, A&A, 523, A77

Pilling S., Seperuelo Duarte E. , da Silveira E. F., Balanzat E., Rothard H., Domaracka A., Boduch P., 2010b, A&A, 509, A87

Pilling S., Andrade D. P. P., Da Silveira E. F., Rothard H., Domaracka A., Boduch P., 2012, MNRAS, 423, 2209

Pilling S., Rocha W. R. M., Freitas F. M., da Silva P. A., 2019, RSC Adv., 9, 28823

Pilling S., Carvalho G. A., Rocha W. R. M., 2022, ApJ, 925, 147

Pilling S., Rocha W. R. M., Carvalho G. A., De Abreu H. A., 2023, Adv. Space Res., 71, 5466

Plainaki C., Milillo A., Mura A., Orsini S., Massetti S., Cassidy T., 2012, 218, 956

Podio L. et al., 2019, A&A, 623, L6

Prialnik D., Bar-Nun A., 1992, A&A, 258, L9

Rachid M. G., Faquine K., Pilling S., 2017, Planet. Space Sci., 149, 83

Rachid M. G., Pilling S., Rocha W. R. M., Agnihotri A., Rothard H., Boduch P., 2020, MNRAS, 494, 2396

Rocha W. R. M., Woitke P., Pilling S., Thi W. F., Jørgensen J. K., Kristensen L. E., Perotti G., Kamp I., 2023, A&A, 673, A70

Rosu-Finsen A., Davies M. B., Amon A., Wu H., Sella A., Michaelides A., Salzmann C. G., 2023, Science, 379, 474

Ruscic B., Bross D. H., 2020, Active Thermochemical Tables (ATcT) values based on ver. 1.122p of the Thermochemical Network 2020. Available at: https://atct.anl.gov/

Ruscic B. et al. 2004, J. Phys. Chem. A, 108, 9979

Ruscic B., Pinzon R. E., Laszewski G. V., Kodeboyina D., Burcat A., Leahy D., Montoy D., Wagner A. F., 2005, J. Phys. Conf. Ser., 16, 561

Smoluchowski R., 1983, Science, 222, 161.

Strazzulla G., Baratta G. A., Leto G., Foti G., 1992, Eur. Phys. Lett. 18, 517

Suh K.-W., Kwon Y.-J., 2013, ApJ, 762, 113

Tachibana S. et al. 2017, Sci. Adv., 3, eaao2538

Teolis B. D., Loeffler M. J., Raut U., Famá M., Baragiola R. A., 2006, ApJ, 644, L141

Teolis B. D., Plainaki C., Cassidy T. A., Raut U., 2017, J. Geophys. Res.: Planets, 122, 1996

Tielens A., Hagen W., 1982, A&A, 114, 245

Vasconcelos F. A., Pilling S., Rocha W. R. M., Rothard H., Boduch P., Ding J. J., 2017a, Phys. Chem. Chem. Phys., 19, 12845

Vasconcelos F. A., Pilling S., Rocha W. R. M., Rothard H., Boduch P., 2017b, Phys. Chem. Chem. Phys., 19, 24154

Vasconcelos F. A, Pilling S., Rocha W. R. M., Rothard H., Boduch P., 2017c, ApJ, 850, 174

Walsh C., Millar T. J., Nomura H., Herbst E., Weaver S. W., Aikawa Y., Laas J. C., Vasyunin A. I., 2014, A&A, 563, A33

Yang Y.-L. et al., 2022, ApJ, 941, L13

Zheng W., Jewitt D., Kaiser R. I., 2006, ApJ, 648. 753

Zheng W., Jewitt D., Kaiser R. I., 2007, Chem. Phys. Letter, 435, 289

APPENDIX A: DETAILS OF THE EMPLOYED COUPLED EQUATIONS

The equations presented below describe the coupled equation's system employed in the current PROCODA code for mapping the evolution of crystalline H_2O ice irradiated by 5 keV electrons at four temperatures ranging from 12 to 90 K. It was considered nine different chemical species within the ice (five observed: H_2, H_2O, O_2, H_2O_2, O_3 (this last, assumed to have very low abundances, below the detection limit of the spectrometer, for calculation purposes); four non-observed: H, O, OH, HO_2), 52 reaction routes including radiation-induced dissociation and bimolecular collision reactions, and 9 radiation-induced desorption reactions, totaling 61 coupled reactions.

d[H]/dt = (-r53–r6–r10–r16–2∗r18–r20–r21–r34–r42–r44–r45–r47–r49 + r5 + r9 + r15 + 2∗r17 + r19 + r22 + r33 + r41 + r43 + r46 + r48 + r50)

d[O]/dt = (-r54–2∗r2–r4–r7–r14–r15–r19–r25–r27–r29–r32–r42–r50–r51 + 2∗r1 + r3 + r8 + r13 + r16 + r20 + r26 + r28 + r30 + r31 + r41 + r49 + r52)

d[H2]/dt = (-r55–r14–r15–r17–r22–r24–r26–r40–r46–r52 + r13 + r16 + r18 + r21 + r23 + r25 + r39 + r45 + r51)

d[OH]/dt = (-r56–r6–r9–2∗r11–r16–r19–r22–r30–r32–r35–r37–r41–r48 + r5 + r10 + 2∗r12 + r15 + r20 + r21 + r29 + r31 + r36 + r38 + r42 + r47)

d[H2O]/dt = (-r57–r5–r7–r9–r13–r21–r23–r28–r36–r38–r51 + r6 + r8 + r10 + r14 + r22 + r24 + r27 + r35 + r37 + r52)

d[O2]/dt = (-r58–r1–r4–r20–r23–r28–r30–r34–r38–r40–r46–r48–r52 + r2 + r3 + r19 + r24 + r27 + r29 + r33 + r37 + r39 + r45 + r47 + r51)

d[HO2]/dt = (-r59–r29–r31–r33–r36–r37–r44–r45–r50 + r30 + r32 + r34 + r35 + r38 + r43 + r46 + r49)

d[H2O2]/dt = (-r60–r8–r10–r12–r25–r27–r35–r39–r43 + r7 + r9 + r11 + r26 + r28 + r36 + r40 + r44)

d[O3]/dt = (-r61–r3–r24–r26–r47–r49 + r4 + r23 + r25 + r48 + r50)

The employed equations for the reaction rates are listed below, where *[i]* is the column density (or concentration) of a given species *i*, *r_i* is the reaction rates, *k_i* is the rate constant, *k_des_i* is the intrinsic desorption rate constant, and Ω_*i* = *[i]*/Σ*[i]* are the surface coverage of the species *i* as a function of time (a dimensionless quantity).

r1 = k1 ∗ [O2]
r2 = k2 ∗ [O] ∗ [O]
r3 = k3 ∗ [O3]
r4 = k4 ∗ [O] ∗ [O2]
r5 = k5 ∗ [H2O]
r6 = k6 ∗ [H] ∗ [OH]
r7 = k7 ∗ [O] ∗ [H2O]
r8 = k8 ∗ [H2O2]
r9 = k9 ∗ [OH] ∗ [H2O]
r10 = k10 ∗ [H] ∗ [H2O2]
r11 = k11 ∗ [OH] ∗ [OH]

r12 = k12 ∗ [H2O2]
r13 = k13 ∗ [H2O]
r14 = k14 ∗ [O] ∗ [H2]
r15 = k15 ∗ [O] ∗ [H2]
r16 = k16 ∗ [H] ∗ [OH]
r17 = k17 ∗ [H2]
r18 = k18 ∗ [H] ∗ [H]
r19 = k19 ∗ [O] ∗ [OH]
r20 = k20 ∗ [H] ∗ [O2]
r21 = k21 ∗ [H] ∗ [H2O]
r22 = k22 ∗ [H2] ∗ [OH]
r23 = k23 ∗ [H2O] ∗ [O2]
r24 = k24 ∗ [H2] ∗ [O3]
r25 = k25 ∗ [O] ∗ [H2O2]
r26 = k26 ∗ [H2] ∗ [O3]
r27 = k27 ∗ [O] ∗ [H2O2]
r28 = k28 ∗ [H2O] ∗ [O2]
r29 = k29 ∗ [O] ∗ [HO2]
r30 = k30 ∗ [OH] ∗ [O2]
r31 = k31 ∗ [HO2]
r32 = k32 ∗ [O] ∗ [OH]
r33 = k33 ∗ [HO2]
r34 = k34 ∗ [H] ∗ [O2]
r35 = k35 ∗ [OH] ∗ [H2O2]
r36 = k36 ∗ [H2O] ∗ [HO2]
r37 = k37 ∗ [OH] ∗ [HO2]
r38 = k38 ∗ [H2O] ∗ [O2]
r39 = k39 ∗ [H2O2]
r40 = k40 ∗ [H2] ∗ [O2]
r41 = k41 ∗ [OH]
r42 = k42 ∗ [H] ∗ [O]
r43 = k43 ∗ [H2O2]
r44 = k44 ∗ [H] ∗ [HO2]
r45 = k45 ∗ [H] ∗ [HO2]
r46 = k46 ∗ [H2] ∗ [O2]
r47 = k47 ∗ [H] ∗ [O3]
r48 = k48 ∗ [OH] ∗ [O2]
r49 = k49 ∗ [H] ∗ [O3]
r50 = k50 ∗ [O] ∗ [HO2]
r51 = k51 ∗ [O] ∗ [H2O]
r52 = k52 ∗ [H2] ∗ [O2]
r53 = k_des_H ∗ Ω_H ∗ [H]
r54 = k_des_O ∗ Ω_O ∗ [O]
r55 = k_des_H2 ∗ Ω_H2 ∗ [H2]
r56 = k_des_OH ∗ Ω_OH ∗ [OH]
r57 = k_des_H2O ∗ Ω_H2O ∗ [H2O]
r58 = k_des_O2 ∗ Ω_O2 ∗ [O2]
r59 = k_des_HO2 ∗ Ω_HO2 ∗ [HO2]
r60 = k_des_H2O2 ∗ Ω_H2O2 ∗ [H2O2]
r61 = k_des_O3 ∗ Ω_O3 ∗ [O3]

APPENDIX B: DETAILS OF THE EMPLOYED SCORE FUNCTION

The considered SF employed in the minimization algorithm during the search of best solution of coupled chemical systems was

$$\begin{aligned}SF \;=\; & p1\ \times \sum \frac{(oH2_{data}-oH2_{model})^2}{oH2_{data}} + p2\ \times \sum \frac{(oH2O_{data}-oH2O_{model})^2}{oH2O_{data}} \\ & + p3\ \times \sum \frac{(oO2_{data}-oO2_{model})^2}{oO2_{data}} + p4\ \times \sum \frac{(oH2O2_{data}-oH2O2_{model})^2}{oH2O2_{data}} \\ & + p5\ \times \sum \frac{(oO3_{data}-oO3_{model})^2}{oO3_{data}} \\ & + p6\ \times [(1-\mathrm{MSC_f}) + (1-\mathrm{MSCo_f}) + (1-\mathrm{MSCo_m})] \\ & + p7\ \times (1-\mathrm{DSC}) + p8\ \times (1-\ \mathrm{SSC})\end{aligned} \tag{2}$$

where the dimensionless parameters *p1* to *p8* in this equation are the weights of each term, used as a tool to search for the best solution during the computational minimization processes. In this equation, the $o[]_{\mathrm{data}}$ and $o[]_{\mathrm{model}}$ are the column density values of given observed species taken from the interpolated experimental data and their respective values calculated by the model, respectively. The model mass similarity criterion (MSC_f) is calculated by comparing the initial column mass of the modeled system to the total column mass of the model at the final modeling time (including both ice and desorbed masses). The observed mass similarity criterion (MSCof and MSCom) is calculated by comparing the experimentally observed column mass to the observed column mass in the model at the final and middle modeling times, respectively. The MSC is then calculated as the average of these three parameters $(MSC_f \times 100\ per\,cent + MSCo_f \times 100\ per\,cent + MSCo_m \times 100\ per\,cent)/3$, which indicates how well the solution of the system matches the observed data. The parameter DSC is the desorption similarity criterion, which is calculated by comparing the input expected desorption yield (based on manuscripts with experimental data) to the total molecular desorption yield computed by the model. The parameter SSC is the slope similarity criterion, which related to the achievement of CE phase in the ice at higher radiation fluence, as described in Pilling et al. (2022).

It is worth noting that the chi-squared function χ^2 (also known as summed CHI2) can be obtained directly from equation [2] by setting p1 = p2 = p3 = p4 = p5 = 1 and p6 = p7 = p8 = 0. This parameter is calculated by comparing the experimental column density (or concentration) data of the observed molecules (H_2, H_2O, O_2, H_2O_2, and O_3) with their modeled column density (or concentration).

This paper has been typeset from a TEX/LATEX file prepared by the author.